THE EFFECTS OF PROMOTERS ON THE SULFUR RESISTANCE OF NO_X STORAGE/REDUCTION CATALYSTS: A DENSITY FUNCTIONAL THEORY INVESTIGATION

A THESIS SUBMITTED TO
THE GRADUATE SCHOOL OF NATURAL AND APPLIED SCIENCES
OF
MIDDLE EAST TECHNICAL UNIVERSITY

BY

RUKAN KOŞAK

IN PARTIAL FULFILLMENT OF THE REQUIREMENTS
FOR
THE DEGREE OF MASTER OF SCIENCE
IN
CHEMISTRY

JULY 2011

Approval of the thesis:

THE EFFECTS OF PROMOTERS ON THE SULFUR RESISTANCE OF NO_X STORAGE/REDUCTION CATALYSTS: A DENSITY FUNCTIONAL THEORY INVESTIGATION

submitted by **RUKAN KOŞAK** in partial fulfillment of the requirements for the degree of **Master of Science in Chemistry Department, Middle East Technical University** by,

Prof. Dr. Canan Özgen
Dean, Graduate School of **Natural and Applied Sciences** _____

Prof. Dr. İlker Özkan
Head of Department, **Chemistry** _____

Assist. Prof. Dr. Daniele Toffoli
Supervisor, **Chemistry, METU** _____

Assist. Prof. Dr. Hande Toffoli
Co-supervisor, **Physics, METU** _____

Examining Committee Members:

Prof. Dr. Şinasi Ellialtıoğlu
Physics, METU _____

Assist. Prof. Dr. Daniele Toffoli
Chemistry, METU _____

Assist. Prof. Dr. Fatih Danışman
Chemistry, METU _____

Assist. Prof. Dr. İrem Erel
Chemistry, METU _____

Assist. Prof. Dr. Salih Özçubukçu
Chemistry, METU _____

Date: **July 29, 2011**

I hereby declare that all information in this document has been obtained and presented in accordance with academic rules and ethical conduct. I also declare that, as required by these rules and conduct, I have fully cited and referenced all material and results that are not original to this work.

Name, Last Name: RUKAN KOŞAK

Signature :

ABSTRACT

THE EFFECTS OF PROMOTERS ON THE SULFUR RESISTANCE OF NO_X STORAGE/REDUCTION CATALYSTS: A DENSITY FUNCTIONAL THEORY INVESTIGATION

Koşak, Rukan

M.Sc., Department of Chemistry

Supervisor : Assist. Prof. Dr. Daniele Toffoli

Co-Supervisor : Assist. Prof. Dr. Hande Toffoli

July 2011, 65 pages

High fossil fuel consumption in transportation and industry results in an increase of the emission of green-house gases. To preserve clean air, new strategies are required. The main intention is to decrease the amount of CO_2 emission by using lean-burn engines while increasing the combustion efficiency and decreasing the fuel consumption. However, the lean-burn engines have high air-to-fuel ratio which complicates the reduction of the oxides of nitrogen, NO_x. The emission of these highly noxious pollutants, NO_x, breeds both environmental and health problems. Thus, new catalytic strategies have been steadily developed. One of these strategies is the NO_x storage and reduction (NSR) catalysts. Since the reduction of the NO_x under excess oxygen condition is very difficult, the NSR catalysts store the NO_x until the end of the lean phase that is subsequently alternated with the rich-fuel phase during which the trapped NO_x is released and reduced.

To develop NSR technology, different storage materials, the coverage of these metals/metal-oxides, support materials, precious metals, temperature, etc. have been widely investigated. In this thesis, the (100) surface of BaO with dopants (K, Na, Ca and La), (100) and (110) surfaces of Li_2O, Na_2O and K_2O are investigated as storage materials. In addition, alkali metal (Li,

Na and K) loaded (001) surface of TiO_2 (titania) anatase is investigated as a support material for the NO_x storage and reduction catalysts. The main aim is to increase the sulfur resistance.

The introduction of the dopants on the BaO (100) surface has increased the stability of the NO_2. The combination of local lattice strain and different oxidation state, which is obtained by the La doped BaO (100) surface, benefit both NO_2 adsorption performance and sulfur tolerance. The binding energies of NO_2 adsorption configurations over the alkali metal oxide (100) and (110) surfaces were higher than the binding energies of SO_2 adsorption configurations. The stability of all of NO_2 adsorption geometries on the alkali metal-loaded TiO_2 (001) surface were higher than the stability of SO_2 adsorption geometries. Increasing basicity enhanced the adsorption of NO_2 molecule.

Keywords: Density Functional Theory (DFT), NO_x Storage/Reduction (NSR), Catalysts, Barium Oxide, Sulfur Poisoning

ÖZ

NO_X DEPOLAMA/İNDİRGEME KATALİZÖRLERİNİN SÜLFÜR DAYANIKLILIĞINA ETKİNLEŞTİRİCİLERİN TESİRİ: BİR YOĞUNLUK FONKSİYONEL TEORİSİ ARAŞTIRMASI

Koşak, Rukan

Yüksek Lisans, Kimya Bölümü

Tez Yöneticisi : Yrd. Doç. Dr. Daniele Toffoli

Ortak Tez Yöneticisi : Yrd. Doç. Dr. Hande Toffoli

Temmuz 2011, 65 sayfa

Ulaşım ve sanayideki yüksek fosil kaynaklı yakıt tüketimi sera gazlarının emisyonunda artışa sebep olmaktadır. Temiz havayı korumak adına yeni stratejilere ihtiyaç duyulmaktadır. Temel amaç düşük-yanışlı motorlar kullanarak CO_2 emisyonunu azaltırken yanma verimini artırıp yakıt tüketimini azaltmaktır. Fakat, düşük-yanışlı motorlar nitrojen oksitlerin, NO_x, indirgenmesini zorlaştıran yüksek hava/yakıt oranına sahiptir. Bu yüksek oranda zehirleyici kirleticilerin emisyonu hem çevresel sorunları hem de sağlık sorunlarını doğurmuştur. Bu sebeple yeni katalitik stratejiler devamlı olarak geliştirilmiştir. Bu stratejilerden bir tanesi de NO_x depolama ve indirgeme (NSR) katalizörleridir. Aşırı oksijen bulunan ortamlarda NO_x'in indirgenmesi zor olduğundan dolayı, NSR katalizörleri yakıt miktarının az olduğu periyotların sonuna kadar NO_x gazlarını depolar ve devamında gelen yakıt miktarının bol olduğu periyotlarda depolanan NO_x geri salınıp indirgenir.

NSR teknolojisini geliştirmek icin farklı depolama materyalleri, bu metal/metal-oksitlerin bulunma miktarları, destekleme materyalleri, soy metaller ve sıcaklık vb. gibi etkenler detaylı olarak araştırılmıştır. Bu tezde, dopant eklenmiş (100) BaO yüzeyi, (100) ve (110) Li_2O, Na_2O ve K_2O yüzeyleri depolama materyali olarak incelenmiştir. Ek olarak, alkali metal (Li,

Na and K) eklenmiş (001) TiO_2 yüzeyi destekleme materyali olarak incelenmiştir.

BaO (100) yüzeyine dopant eklenmesi NO_2'nin kararlılığını arttırmıştır. Farklı yükseltgenme basamağı ve kısmi örgü geriniminin kombinasyonu, ki bunlar La dopant maddesinin eklendigi BaO (100) yüzeyinde elde edilmiştir, hem NO_2 tutunma performansına hem de sülfür toleransına yarar sağlamıştır. Alkali metal oksit (100) ve (110) yüzeyleri üzerindeki NO_2 tutunma konfigürasyonlarının bağlanma enerjileri SO_2 tutunma konfigürasyonlarından büyüktür. NO_2'nin alkali metal eklenmiş TiO_2 (001) yüzeyi üzerindeki bütün bağlanma konfigürasyonlarının kararlılığı SO_2'nin bağlanma konfigürasyonlarının kararlılığından yüksektir. Artan bazlık kuvveti NO_2 tutunumunu geliştirmiştir.

Anahtar Kelimeler: Yoğunluk Fonksiyoneli Teorisi, NO_x Depolama/İndirgeme, Katalizör, Baryum Oksit, Sülfür Kirliliği

To my family

ACKNOWLEDGMENTS

I would like to express my sincere gratitude to my supervisor Assist. Prof. Dr. Daniele Toffoli and my co-supervisor Assist. Prof. Dr. Hande Toffoli for their guidance, encouragement, support, invaluable assistance on research and willingness to share their insight and wisdom throughout this academic exploration.

I am heartily indebted to Ruslan Hummatov and Uğur Bozkaya for fruitful discussions and their cooperation.

Many thanks to my numerous friends: Dilay Kızışar, Eray Biniş, Irmak Yay, İlker Demiroğlu, H. Doğa Öner, Mehmet Kabar, Meryem Karabulut, N. Okan (Rıza) Çiftçi, Onur Özdil, Ömer Sarı, Tuğba Orhan, Uğur Elmas, Yasemin Yaman, Zafer Öztürk, for their encouragement and support. I would like to individually thank to my roommate Elif Ṣükran Soyaslan for her precious friendship and keeping me in a good mood.

Last but not least, I would like to express my gratitude to my family for their moral support and patience during my study, especially to my sister Elif Erdoğan.

This work is financially supported by TÜBİTAK (The Science and Technological Research Council of Turkey) (Grant no:108T706).

TABLE OF CONTENTS

LIST OF TABLES

TABLES

LIST OF FIGURES

FIGURES

CHAPTER 1

INTRODUCTION

Increasing emission of green-house gases due to high fuel consumption of gasoline engines and industrial applications requires new strategies for preserving clean air. There are several regulations which are set to control carbon dioxide emissions. The main intention is to decrease the amount of CO_2 emission by using lean-burn or diesel engines in conjunction with the increase of combustion efficiency and the decrease of the fuel consumption. Unfortunately, the lean-burn engines have high air-to-fuel ratio which causes the three-way catalysts [1] to be ineffective for the reduction of oxides of nitrogen (NO_x).

The emission of the highly noxious and toxicologically most significant pollutants such as nitric oxide and nitrogen dioxide, breeds both environmental and health problems. One of the most hazardous environmental problems due to the increasing amount of NO_x in air is that it gives rise to global warming [2] and acid rains [3-5]. In addition, when oxides of nitrogen react with other pollutants in air, they produce toxic chemicals which mostly lead plant growth to cease [3]. As the amount of the NO_x exposure varies, the severity of the health problems also varies. Small amount of NO_x can cause nausea, shortness of breath and fluid formation in lungs [6]. When the amount of NO_x exposure increases, the health problems become more severe. Burning spasms, visual impairment, swelling of throat, reduced oxygen intake, respiratory problems and larger amount of fluid formation in lungs are some of the examples of severe health problems due to excess amount of NO_x [5].

Fossil fuel combustion is the fundamental source of the nitrogen oxides [6]. Earlier studies showed that most of the NO_x emission was due to transportation [6, 7]. There are several regulations which have been proposed to control NO_x emission like the ones for CO_2 emission and they vary depending on countries. For example, the legislation for diesel vehicles in the

European Union (EU) countries is different from the legislation in the United States (US) since diesel cars represent almost half of all cars in the EU countries, whereas they represent less than 5% of all cars in the USA [6, 8]. The NO_x emission standards have been adopted by European countries since 1992 [9]. In order to prevent air pollution due to the growing number of automobiles, subsequent emission standards set lower emission limits for NO_x emission of diesel cars [8-10] (Table 1.1).

Table 1.1: Overview of NO_x emission limits (mg/km) in Europe for Gasoline and Diesel cars with implementation year [8, 9].

Emission Standards	Oxides of Nitrogen (NO_x)	
	Diesel Cars	Gasoline Cars
Euro 1 (1992)	900	620
Euro 2 (1996)	670	350
Euro 3 (2000)	500	150
Euro 4 (2005)	250	80
Euro 5 (2009)	180	70
Euro 6 (2014)	80	70

New catalytic strategies, determined both experimentally and theoretically, have been steadily developed in order to unravel the issues due to NO_x emission. One of these strategies is the NO_x storage and reduction (NSR) catalysts.

1.1 NO_x Storage-Reduction Catalysts

The NSR technology, which was brought into practice by Toyota in the early 1990s, has a cyclic working mechanism [11-13]. Lean-burn engines operate in conditions which switch between a long lean phase (excess oxygen condition) and a very short rich-fuel phase. Since the reduction of NO_x under excess oxygen condition is very difficult, the NSR catalysts store NO_x until the end of the lean phase that is subsequently alternated with the rich-fuel phase during which the trapped NO_x is released and reduced [10-13]. For sustaining this cyclic working mechanism, the NSR catalysts consist of two main parts; i) trapping part and ii) reducing and releasing part.

To be able to fulfill the first objective, the NSR catalysts require some fundamental components. Regarding the storage mechanism, as illustrated in Figure 1.1, NO is first oxidized to

NO_2 over the noble metal (Pt) surface under lean-burn conditions. For this reason, the first component is the oxidation component; mostly a noble metal (e.g. Pt, Rh [10]). The second component is the storage component; commonly the alkali and/or alkaline earth metals/metal-oxides (e.g. K, Ba, BaO, MgO etc.) and the last one is the high surface area support (e.g. γ-Al_2O_3, TiO_2), [10, 13]. These given materials were most extensively studied due to their potential applications as NO_x storage materials. For the second objective, mostly hydrocarbons (HCs) (C_3H_8, C_3H_6 etc. [12, 14]) and CO or H_2 (over the noble metal sites) were used to reduce NO_x [15]. The final products are CO_2, N_2 and H_2O [15].

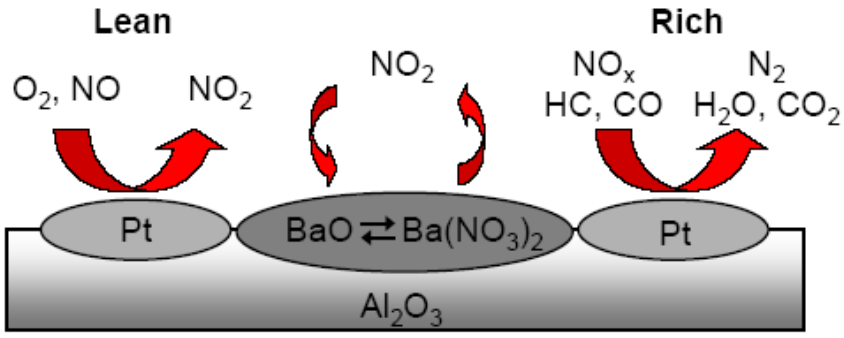

Figure 1.1: Schematic representation of NO_x storage and reduction mechanism over $Pt/BaO/Al_2O_3$ under lean and rich conditions.

The general consensus is that the catalytic process begins with the oxidation of NO to NO_2 by the noble metal under conditions of excess oxygen [16, 17]. This oxidation reaction is the key of the storage of NO in the form of surface nitrites. The exhaust gas also contains NO_2 molecule and the direct storage of this compound yields surface nitrites as well and the active surface anions (O^{-2}_{surf}) lead to the formation of surface nitrates. The studies revealed that the NO_x storage can occur through single and pairwise NO_2 adsorption (which is the formation of nitrite-nitrite, nitrite-nitrate and nitrate-nitrate pairs) on the surface [18, 19]. As stated before, the catalytic process continues with the reduction of surface nitrites and nitrates to N_2 by the hydrocarbons (HCs) and H_2 or CO [20, 21] under fuel-rich conditions.

There have been several studies varying in terms of storage materials, the coverage of these metals/metal-oxides, support materials, precious metals, temperature, etc. [6, 12, 22-25]. In conjunction with the investigation of some of these factors, most of the studies analyzed the mechanism of storage and reduction process [10, 14, 26-29]. In order to scrutinize the mech-

anism, one should consider each step; possible reactions involved in adsorption, oxidation, and reduction of NO_x.

1.2 The Components of the NO_x Storage-Reduction Catalysts

Before investigating the key parts of the mechanism of the NSR concept, characteristics of the components of the NSR catalysts should to be examined. The selection of the storage material is one of the most important parts of the NSR concept since the very first step of the NSR is NO_x storage on metal/metal-oxide surface. In order to achieve high activity, a highly dispersed storage material is critical. Additionally, the cycle of trapping and reducing the NO_x shares the importance because the efficiency of the catalysts strongly relies on the reversible adsorption capacity of the storage material.

The choice of the support material is one of the other important parts of the NSR concept even though the amount of the adsorbed NO_x on the support material is often negligible [14]. The studies showed that the modifications of the support material can improve the NSR activity since the support enhances the performance of the storage components and leads to higher storage capacity [12, 30]. Moreover, the choice of the support material affects the removal efficiency [30].

Since the precious metal is the promoter of the NO_x adsorption on the storage and support material, and the oxidation of NO to NO_2, the efficiency of the NSR catalysts also depends on the properties of the noble metal [31]. As a result, understanding the essential characteristics of the storage materials, support and precious metal assists to enhance the NO_x storage capacity.

1.2.1 The Storage Material

Due to the acidity of NO_x species, the stability of the adsorbate is determined by the basicity of the substrate [11, 20, 21] as shown in Figure 1.2 [11]. The electron donating property (basicity) designates the charge transfer at the surface. It is known that for chemisorption, relatively high charge transfer is required due to the binding character. Within the groups of IA and IIA, the basicity of the metallic oxides increases going down the group. In addition, high

hydrothermal stability of their oxides and being able to form stable peroxo species are some of the beneficial characteristics of these highly basic metals [11, 22]. Consequently, barium oxide has been widely investigated as a storage material of the NSR catalyst and it was found that BaO surface has high reactivity toward NO_x [21]. Furthermore, studies revealed that BaO is not only one of the most suitable substrates for single NO_x adsorption, but also a promoter of the pairwise NO_x adsorption [19, 20].

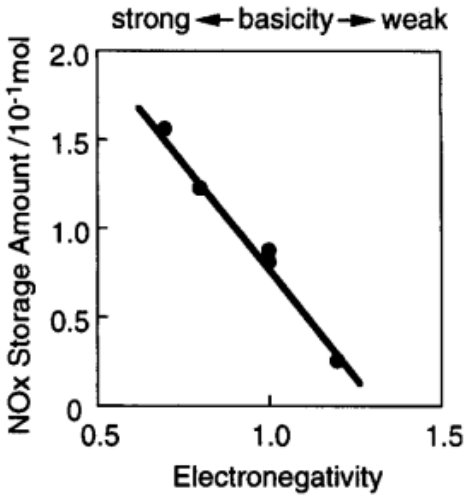

Figure 1.2: The relation between electronegativity of the storage materials and the NO_x storage amount (Catalyst: Pt/(NO_x storage compound)/Al_2O_3, Temperature: 523 K) [11].

Although barium oxide is the most commonly used storage material in several experimental and theoretical studies [15-17, 25-29], it is found that K_2O is more efficient as a storage material than BaO [13, 15]. An earlier study reported that the storage capacity of Pt-K/Al_2O_3 is higher than the Pt-Ba/Al_2O_3 at temperatures up to 673 K [10, 15]. Moreover, K_2O has an essential role on increasing the removal efficiency. The retention of the NO_x stored (until the fuel-rich period) is very important. K_2O enables the system to possess sufficient interaction strength and increases the efficiency of the process [13, 16].

Further investigations were done to examine the limitations of barium oxide [15-18, 21, 27, 28] and it was found that some of these limitations such as poor sulfur durability and low thermal stability can be overcome by using potassium oxide and barium oxide together [16]. The only deficiency of the potassium oxide is that even though it enhances the storage capacity of the barium oxide and alumina (Al_2O_3), it does not have high hydrothermal stability which is crucially required for the storage materials [16]. Both of the catalysts had lower storage

capacity due to water vapor, but they preserved their storage capacity better when they were co-loaded [15, 16]. Consequently, their dual usage is considered to be more advantageous.

The investigations revealed that even though exactly the same mechanism for the adsorption of different adsorbates over various surfaces were observed [20], high variation of the stability and the adsorption efficiency of the adsorbates were the case.

1.2.1.1 Effect of the Coverage

The efficiency of the NSR catalysts strongly depends on the amount of storage metal/metal-oxide on the support material. There is considerable difference between the amount of adsorbed NO_x on pure alumina and barium oxide and potassium oxide loaded on alumina [15, 16]. It was found that increasing the coverage of the storage material increases the amount of adsorbed NO_x and when K_2O and BaO are co-loaded, K_2O activates both BaO and γ-Al_2O_3 toward formation of surface nitrates [13, 16].

An experimental study investigated the effect of the BaO coverage on the amount of the adsorbed NO_x and the results showed that higher extent of surface nitrite and nitrate formation was observed as the BaO coverage increased form 8 to 20 wt % [18]. Moreover, it was suggested that there is a relation between the amount of evolved NO_2 and the surface area of the catalyst. Based on this suggestion, it can be deduced that the amount of the stored NO_2 is proportional to the amount of the impregnation with BaO on the γ-Al_2O_3 surface [18]. In another study, high coverage condition gave rise to pairwise adsorption and subsequently increased the adsorption efficiency [29].

1.2.2 The Support Material and the Noble Metal

Several studies revealed that despite being an indirect participant in the catalytic processes, the NO_x adsorption and desorption properties of the storage materials depend remarkably on the support material [13, 16, 29, 30]. Support material not only supplies high surface area, but also provides storage sites at low temperatures. For this reason, the selection of the support material should be considered carefully. The reason why most of the studies included γ-Al_2O_3 is that among many support materials, it is the one with highest NO_x storage capacity. At room temperature, nitrate formation on both support material and the storage material is

detected [18, 30].

Schmitz et al. conducted several experiments on the effect of the precious metal on NO_x adsorption process [29]. The precious metal catalyzes the oxidation of the NO to NO_2 and activates the support material [29, 31]. At high temperatures, NO was oxidized to NO_2 and mainly nitrates were observed with an increase of the amount of adsorbed NO_x [29]. This was due to the presence of the precious metal.

Considering the effect of platinum usage, the amount of the NO_x species were analyzed [30]. It was found that although the presence of platinum resulted in an increase of the amount of adsorbed NO_x, it did not appreciably change the nature of the stored oxides of nitrogen. On the other hand, it reduced the thermal stability of the NO_x species. This result indicates that the noble metal is essential for the reduction and removal of NO_x as well [14].

1.3 Competition between the adsorbates

The limitations of trapping NO_x were overcome by varying the storage components. There have been several studies about the effect of the storage component on the catalytic reactivity and it was found that the limitations vary from metal to metal [15-18]. The most common limitation is the selectivity of the metal/metal-oxide [21].

Considering the main reactive components, the exhaust gas contains CO_x, H_2O, SO_x and NO_x [21], hence there is a competition between these adsorbates for adsorption on the surface of the storage material. The possible products are desired nitrites, and nitrates and unwanted carbonates, sulfates, hydroxides and peroxides [21, 27]. The most important competition is between NO_x, CO_x and SO_x species.

1.3.1 CO_x Poisoning

For all the storage materials, the stability of the surface species formed is in the order $NO_2^- \approx CO_3^{2-} < NO_3^- < SO_4^{2-}$ [21]. Although CO_x and NO_x molecules are competing for the same binding sites and all adsorbates form stable surface species on the surface of the metal, it was suggested that the presence of CO_2 does not substantially affect the adsorption efficiency of the NO_x [21].

In a previous publication, it was suggested that CO_2 in the exhaust gas covers the surface of the storage material [28]. The results of this study came with an unexpected conclusion that carbon dioxide significantly affects the amount of stored NO_x on BaO and it can block a large part of the available binding sites. In order to further investigate this unexpected conclusion, NO_2 storage experiments on a $BaCO_3$ sample were conducted [27]. The results showed that the intensities of NO_x species are lower than BaO sample due to the low accessible surface area. On the other hand, Broqvist et al. [20] and Karlsen et al. [21] concluded that the surface carbonates are not the major problem due to the fact that surface CO_x formation is unstable toward surface nitrite/nitrate formation since their thermodynamic stability is lower [20] and their formation energy is higher than the surface nitrites/nitrates [21]. It was suggested that the formation of the surface carbonates is possible and these carbonates can inhibit the NO_x adsorption, but not irreversibly [20, 21].

1.3.2 SO_x Poisoning

The surface sulfites/sulfates are severely problematic since the formation energies of both sulfite and sulfate over the surface of the storage material are higher than formation energies of the nitrite and nitrate species [28]. SO_x species cause the inhibition of NO_x storage and reduction, and lessen the efficiency of the NSR catalyst since they have the highest thermodynamic stability [20, 21]. This inhibition is called *sulfur poisoning*.

Sulfur poisoning affects the efficiency of the precious metal, the storage material and the support [20, 21, 32]. Studies confirmed that SO_2 molecule gets oxidized (like NO) on the precious metal sites and then is absorbed by the substrate. It inhibits the NO_x adsorption by forming strongly chemisorbed sulfates on the available binding sites [21]. Moreover, the formation of sulfur species on the precious metal sites decreases the reduction capacity of this metal during rich fuel conditions [32]. As a consequence, the amount of adsorbed NO_x over the catalyst decreases appreciably after each cycle since the binding sites would be occupied with the unreduced NO_x and SO_x from the former cycle [32].

In order to increase the efficiency of the NSR catalysts, sulfur poisoning needs to be decreased without varying the temperature and causing thermal deactivation. This can be achieved by making surface SO_x species weaker or simply making NO_x adsorption more stable.

Although it is well known that barium oxide is a highly effective promoter of pairwise adsorption [19, 20] and therefore it is widely studied as a storage material, a DFT investigation on the impact of dopants on the NO_x storage and reduction performance of BaO has not been considered yet. In this thesis the effect of the different dopants (K, Na, Ca and La) on BaO (100) surface on sulfur poisoning has been investigated. Secondly, alkali metal oxides Li_2O through K_2O were chosen as the storage component and the effect of the basicity of the storage material on sulfur poisoning is investigated. Lastly, to increase the SO_x tolerance while retaining an acceptable NO_x storage capacity, alkali metal (Li, Na and K) loaded TiO_2 surfaces are studied.

This thesis consists of four chapters. In Chapter 2, density functional theory (DFT) is introduced. In the third chapter, results of DFT calculations are discussed, and a summary is provided in the conclusion section.

CHAPTER 2

DENSITY FUNCTIONAL THEORY

Density Functional Theory (DFT) is a computational method which is used for investigating the properties of many-particle systems. It does not take as the target quantity to be the quantum mechanical wave functions, but instead, it relies on electron density. This is because the wave function is practically impossible to compute for any system of importance whereas the electron density proves to be easier to handle.

2.1 The Schrödinger Equation

In principle, all desired knowledge about any system can be acquired from the quantum mechanical wave function which can be obtained by solving the Schrödinger equation of the complete many-particle system. A fundamental postulate of quantum mechanics is that a wave function, Ψ, can be found for every chemical system and suitable operators that act on eigenfunction Ψ return the observable properties of the system. The operator that returns the energy of the system, E, as an eigenvalue, is called Hamiltonian operator, $\hat{H}$, and the Schrödinger equation can be written as:

$$\hat{H}\Psi = E\Psi \tag{2.1}$$

The general form of the Hamiltonian operator includes five parts which are the kinetic energies of the electrons and nuclei, the inter-electronic and inter-nuclear repulsions, and lastly the attraction of electrons to the nuclei. This can be expressed in mathematical notation in the

following way:

$$\hat{H} = -\frac{\hbar^2}{2m_e}\sum_{i=1}^{N_e}\nabla^2_{\vec{r_i}} - \frac{\hbar^2}{2m_n}\sum_{I=1}^{N_n}\nabla^2_{\vec{R_I}} + \frac{1}{2}\frac{e^2}{4\pi\epsilon_0}\sum_{i}^{N_e}\sum_{j\neq i}^{N_e}\frac{1}{|\vec{r_i}-\vec{r_j}|} + \frac{1}{2}\frac{e^2}{4\pi\epsilon_0}\sum_{I}^{N_n}\sum_{J\neq I}^{N_n}\frac{Z_I Z_J}{|\vec{R_I}-\vec{R_J}|} - \frac{e^2}{4\pi\epsilon_0}\sum_{i=1}^{N_e}\sum_{I=1}^{N_n}\frac{Z_I}{|\vec{r_i}-\vec{R_I}|} \quad (2.2)$$

where $\vec{R_I}$ denotes the position of the I^{th} nucleus, $\vec{r_i}$ is the position of the i^{th} electron and Z_I is the atomic number of the I^{th} nucleus. The factor of 1/2 in the third and fourth terms has been included to avoid double-counting.

Even for the He atom, solving the Schrödinger equation analytically is impossible since the description of interacting many-particle systems is very complicated. For this reason, approximations concerning the Schrödinger equation carry the greatest importance.

2.1.1 The Born-Oppenheimer Approximation

As can be seen in the Eq. (2.2), the Hamiltonian operator includes pairwise attraction and repulsion terms. This suggests that none of the particles moves independently of all the others. It is a fact that the nuclei are much heavier than electrons and therefore they are moving much more slowly than electrons. If the positions of the nuclei vary, then the electrons adjust their positions accordingly. In light of this information, Born and Oppenheimer proposed an excellent approximation that treats the motion of the nuclei and electrons separately [33]. The approximation also states that the potential energy term due to the nuclei-nuclei interaction can be regarded as a simple constant.

The many-particle wave function can be divided into two parts because the motion of the nuclei and electrons are adiabatically separated. This can be written as:

$$\Psi(\mathbf{r},\mathbf{R}) = \Phi_m(\mathbf{R})\Psi^{el}(\mathbf{r},\mathbf{R}) \quad (2.3)$$

where $\mathbf{r}$ and $\mathbf{R}$ are the electronic and nuclear coordinates respectively, $\Phi_m(\mathbf{R})$ is the nuclear wave function and $\Psi^{el}(\mathbf{r},\mathbf{R})$ is the electronic wave function which describes the motion of the electrons with fixed nuclear coordinates. The electronic Schrödinger equation can be written as:

$$\hat{H}^{el}\Psi^{el}(\mathbf{r},\mathbf{R}) = E^{el}(\mathbf{R})\Psi^{el}(\mathbf{r},\mathbf{R}) \quad (2.4)$$

where $\hat{H}^{el}$ is the electronic Hamiltonian and contains the kinetic energies of the electrons ($\hat{T}_{el}$), the attraction of electrons to the nuclei ($\hat{V}_{ne}$), and the inter-electronic repulsions ($\hat{V}_{ee}$). The eigenvalues of this electronic Schrödinger equation are the electronic energies, E^{el} which have a parametric dependence on the nuclear coordinates. If atomic units are chosen, the electronic Hamiltonian can be written as:

$$\hat{H}^{el} = -\frac{1}{2}\sum_{i=1}^{N_e}\nabla^2_{\vec{r_i}} + \frac{1}{2}\sum_{i}^{N_e}\sum_{j\neq i}^{N_e}\frac{1}{|\vec{r_i}-\vec{r_j}|} - \sum_{i=1}^{N_e}\sum_{I=1}^{N_n}\frac{Z_I}{|\vec{r_i}-\vec{R_I}|}. \tag{2.5}$$

2.2 The DFT Method

The focus of ab-initio quantum chemistry methods is to find the complicated electronic wave function in Eq. (2.4) without any assumption on the Hamiltonian. The computational effort for evaluating such a complex electronic wave function is very high since for an N-particle system, Ψ^{el} is a function of 3N coordinates (if the spin coordinate is neglected). A possible solution to this problem was introduced by Hohenberg and Kohn [34]. Their theorems which gave birth to density functional theory (DFT) states that it is not necessary to calculate the 3N dimensional electronic wave function for an exact description of the system. The knowledge of the electron density, $\rho(\vec{\mathbf{r}})$, which is a function of only three variables is enough for an exact description of the system.

In density functional theory, the term *functional* is used because the energy is written as a functional of the electronic density. A functional maps a function to a number whereas a function maps a number to a number:

$$f(x) : x \rightarrow y \;\; (Function) \tag{2.6}$$

$$F[f(x)] : f(x) \rightarrow y \;\; (Functional) \tag{2.7}$$

A simple example of functional is the energy of the system:

$$E[\Psi] = \langle\Psi|\hat{H}|\Psi\rangle \tag{2.8}$$

where Ψ is the wave function.

2.2.1 The Electron Density

In DFT, the energy of a system is defined as the functional of the electron density which is a function that depends only on three variables (the spatial coordinates) **regardless of the number of electrons**. For a many-particle system, the electron density, $\rho(\vec{\mathbf{r}})$, can be found by calculating the expectation value of the single-particle density operator, $\hat{\rho}(\vec{\mathbf{r}})$:

$$\hat{\rho}(\vec{\mathbf{r}}) = \sum_{i=1}^{N} \delta(\vec{\mathbf{r}} - \vec{\mathbf{r}}_i). \tag{2.9}$$

using the many-body wave function:

$$\rho(\vec{\mathbf{r}}) = \langle \Psi(\vec{\mathbf{r}}_1, \ldots, \vec{\mathbf{r}}_N) | \hat{\rho}(\vec{\mathbf{r}}) | \Psi(\vec{\mathbf{r}}_1, \ldots, \vec{\mathbf{r}}_N) \rangle = \sum_{i=1}^{N} \int \delta(\vec{\mathbf{r}} - \vec{\mathbf{r}}_i) |\Psi(\vec{\mathbf{r}}_1, \vec{\mathbf{r}}_2, \ldots, \vec{\mathbf{r}}_N)|^2 d\vec{\mathbf{r}}_1 d\vec{\mathbf{r}}_2 \ldots d\vec{\mathbf{r}}_N$$
$$= \int |\Psi(\vec{\mathbf{r}}, \vec{\mathbf{r}}_2, \ldots, \vec{\mathbf{r}}_N)|^2 d\vec{\mathbf{r}}_2 d\vec{\mathbf{r}}_3 \ldots d\vec{\mathbf{r}}_N + \int |\Psi(\vec{\mathbf{r}}_1, \vec{\mathbf{r}}, \ldots, \vec{\mathbf{r}}_N)|^2 d\vec{\mathbf{r}}_1 d\vec{\mathbf{r}}_3 \ldots d\vec{\mathbf{r}}_N + \ldots \tag{2.10}$$

This equation can be simplified as:

$$\rho(\vec{\mathbf{r}}) = N \int |\Psi(\vec{\mathbf{r}}, \vec{\mathbf{r}}_2, \ldots, \vec{\mathbf{r}}_N)|^2 d\vec{\mathbf{r}}_2 d\vec{\mathbf{r}}_3 \ldots d\vec{\mathbf{r}}_N \tag{2.11}$$

where $\vec{r}$ is the spatial variable. The result of the integration of the electron density over all space is the number of electrons:

$$\int \rho(\vec{\mathbf{r}}) d\vec{\mathbf{r}} = N \tag{2.12}$$

as a consequence of the normalization of the wave function Ψ.

2.2.2 Energy as a Functional of the Electron Density

The advantage of DFT is that the electronic wave function is no longer the fundamental variable of interest, instead, the electron density is used to describe all terms of the total ground state energy of the system. In order to obtain the energy of the system, the expectation value of the electronic Hamiltonian:

$$\hat{H}^{el} = \hat{T}_{el} + \hat{V}_{ee} + \hat{V}_{ne} \tag{2.13}$$

should be calculated using the many-particle wave function:

$$\langle \Psi(\vec{\mathbf{r}}_1, \ldots, \vec{\mathbf{r}}_N) | \hat{H}^{el} | \Psi(\vec{\mathbf{r}}_1, \ldots, \vec{\mathbf{r}}_N) \rangle = \langle \Psi(\vec{\mathbf{r}}_1, \ldots, \vec{\mathbf{r}}_N) | \hat{T}_{el} + \hat{V}_{ee} + \hat{V}_{ne} | \Psi(\vec{\mathbf{r}}_1, \ldots, \vec{\mathbf{r}}_N) \rangle. \tag{2.14}$$

This expectation value can be divided into three parts and the electronic kinetic energy part can be expressed as:

$$\langle\Psi(\vec{\mathbf{r}}_1,\ldots,\vec{\mathbf{r}}_N)|\hat{T}_{el}|\Psi(\vec{\mathbf{r}}_1,\ldots,\vec{\mathbf{r}}_N)\rangle = T_{el} = -\frac{1}{2}\sum_{i=1}^{N}\int \Psi^*(\vec{\mathbf{r}}_1,\ldots,\vec{\mathbf{r}}_N)\nabla^2_{\vec{\mathbf{r}}_i}\Psi(\vec{\mathbf{r}}_1,\ldots,\vec{\mathbf{r}}_N). \quad (2.15)$$

In order to evaluate the expectation value of the kinetic energy part, an important assumption needs to be done since there is a derivative term in the kinetic energy operator and for this reason kinetic energy cannot be written in terms of the density. The assumption states that the density can be written in terms of single-particle (Kohn-Sham) orbitals, $\phi_n(\vec{\mathbf{r}})$ of a fictitious non-interacting electron system, characterized by the same density $\rho(\vec{\mathbf{r}})$:

$$\rho(\vec{\mathbf{r}}) = \sum_{n}^{N_e}|\phi_n(\vec{\mathbf{r}})|^2. \quad (2.16)$$

By using Eq. (2.16), the electronic kinetic energy term can be written as:

$$T_{el} = -\frac{1}{2}\sum_{n}^{N_e}\int \phi_n^*(\vec{\mathbf{r}})\nabla^2\phi_n(\vec{\mathbf{r}})d\vec{\mathbf{r}} + \Delta T_{el} \quad (2.17)$$

where a correction term, say ΔT_{el}, must be added to account for the difference between the true kinetic energy and the single-particle kinetic energy.

The next term in the electronic Hamiltonian of Eq. (2.5) is the inter-electronic repulsion, $\hat{V}_{ee}$. The expectation value of the electron-electron potential energy operator can be expressed as:

$$\langle\Psi(\vec{\mathbf{r}}_1,\ldots,\vec{\mathbf{r}}_N)|\hat{V}_{ee}|\Psi(\vec{\mathbf{r}}_1,\ldots,\vec{\mathbf{r}}_N)\rangle = V_{ee} = \frac{1}{2}\sum_{i}^{N_e}\sum_{j\neq i}^{N_e}\int \frac{1}{|\vec{\mathbf{r}}_i-\vec{\mathbf{r}}_j|}|\Psi(\vec{\mathbf{r}}_1,\ldots,\vec{\mathbf{r}}_N)|^2 d\vec{\mathbf{r}}_1\ldots d\vec{\mathbf{r}}_N. \quad (2.18)$$

Since both of the summations are over electrons, when the terms are expanded over the electron indices, V_{ee} becomes:

$$V_{ee} = \frac{1}{2}\Big[\iint \frac{1}{|\vec{\mathbf{r}}_1-\vec{\mathbf{r}}_2|}d\vec{\mathbf{r}}_1 d\vec{\mathbf{r}}_2\int|\Psi(\vec{\mathbf{r}}_1,\ldots,\vec{\mathbf{r}}_N)|^2 d\vec{\mathbf{r}}_3 d\vec{\mathbf{r}}_4\ldots d\vec{\mathbf{r}}_N + \iint \frac{1}{|\vec{\mathbf{r}}_1-\vec{\mathbf{r}}_3|}d\vec{\mathbf{r}}_1 d\vec{\mathbf{r}}_3\int|\Psi(\vec{\mathbf{r}}_1,\ldots,\vec{\mathbf{r}}_N)|^2 d\vec{\mathbf{r}}_2 d\vec{\mathbf{r}}_4\ldots d\vec{\mathbf{r}}_N + \ldots\Big]. \quad (2.19)$$

It is clear that this term cannot be written in terms of the single-particle density, instead, it can only be expressed in terms of the two-particle density, $\rho(\vec{\mathbf{r}},\vec{\mathbf{r}'})$. In order to show this, we first calculate the expectation value of the two-particle density operator, $\hat{\rho}(\vec{\mathbf{r}},\vec{\mathbf{r}'})$:

$$\hat{\rho}(\vec{\mathbf{r}},\vec{\mathbf{r}'}) = \sum_{i}^{N_e}\sum_{j}^{N_e}\delta(\vec{\mathbf{r}}-\vec{\mathbf{r}}_i)\delta(\vec{\mathbf{r}'}-\vec{\mathbf{r}}_j) \quad (2.20)$$

and the result is:

$$\rho(\vec{\mathbf{r}}, \vec{\mathbf{r}'}) = \frac{N_e(N_e-1)}{2} \int |\Psi(\vec{\mathbf{r}}, \vec{\mathbf{r}'}, \vec{\mathbf{r}}_3, \ldots, \vec{\mathbf{r}}_N)|^2 d\vec{\mathbf{r}}_3 d\vec{\mathbf{r}}_4 ... d\vec{\mathbf{r}}_N. \tag{2.21}$$

Finally, the electron-electron potential energy can be written as:

$$V_{ee} = \frac{1}{2}\frac{2}{N_e(N_e-1)}\Big[\iint \frac{\rho(\vec{\mathbf{r}}_1, \vec{\mathbf{r}}_2)}{|\vec{\mathbf{r}}_1 - \vec{\mathbf{r}}_2|} d\vec{\mathbf{r}}_1 d\vec{\mathbf{r}}_2 + \iint \frac{\rho(\vec{\mathbf{r}}_1, \vec{\mathbf{r}}_3)}{|\vec{\mathbf{r}}_1 - \vec{\mathbf{r}}_3|} d\vec{\mathbf{r}}_1 d\vec{\mathbf{r}}_3 + \ldots \Big]. \tag{2.22}$$

By rearranging the variables in Eq. (2.22), we arrive at the result:

$$V_{ee} = \frac{1}{2} \iint \frac{\rho(\vec{\mathbf{r}}, \vec{\mathbf{r}'})}{|\vec{\mathbf{r}} - \vec{\mathbf{r}'}|} d\vec{\mathbf{r}} d\vec{\mathbf{r}'} \tag{2.23}$$

where $\rho(\vec{\mathbf{r}}, \vec{\mathbf{r}'})$ represents the probability of one electron being at position $\vec{\mathbf{r}}$ and the other one at $\vec{\mathbf{r}'}$. The two-particle density term makes the many-particle problem very difficult to solve. $\rho(\vec{\mathbf{r}}, \vec{\mathbf{r}'})$ could be written as the product of single-particle densities if the two electrons were completely uncorrelated. It is therefore natural to write

$$\rho(\vec{\mathbf{r}}, \vec{\mathbf{r}'}) = \rho(\vec{\mathbf{r}})\rho(\vec{\mathbf{r}'}) + \Delta\rho(\vec{\mathbf{r}}, \vec{\mathbf{r}'}) \tag{2.24}$$

where the correction, $\Delta\rho(\vec{\mathbf{r}}, \vec{\mathbf{r}'})$, is due to the correlated motion of the electrons. The electron-electron potential energy term of Eq. (2.23) can therefore be written as:

$$V_{ee} = \frac{1}{2} \iint \frac{\rho(\vec{\mathbf{r}})\rho(\vec{\mathbf{r}'})}{|\vec{\mathbf{r}} - \vec{\mathbf{r}'}|} d\vec{\mathbf{r}} d\vec{\mathbf{r}'} + \Delta V_{ee} \tag{2.25}$$

where ΔV_{ee} represents all the non-classical corrections to the electron-electron potential energy.

The last term is the attraction of electrons to the nuclei, $\hat{V}_{ne}$. Since the operator does not have any derivative term, its expectation value can simply be written as:

$$\langle \Psi(\vec{\mathbf{r}}_1, \ldots, \vec{\mathbf{r}}_N) | \hat{V}_{ne} | \Psi(\vec{\mathbf{r}}_1, \ldots, \vec{\mathbf{r}}_N) \rangle = V_{ne} = -\sum_{i=1}^{N_e} \sum_{I=1}^{N_I} \int \frac{Z_I}{|\vec{\mathbf{r}}_i - \vec{\mathbf{R}}_I|} |\Psi(\vec{\mathbf{r}}_1, \ldots, \vec{\mathbf{r}}_N)|^2 d\vec{\mathbf{r}}_1 \ldots d\vec{\mathbf{r}}_N. \tag{2.26}$$

If the summation is expanded over the electronic indices, then V_{ne} can be written as:

$$V_{ne} = -\sum_{I=1}^{N_I} \Big[\int \frac{Z_I}{|\vec{\mathbf{r}}_1 - \vec{\mathbf{R}}_I|} |\Psi(\vec{\mathbf{r}}_1, \ldots, \vec{\mathbf{r}}_N)|^2 d\vec{\mathbf{r}}_1 d\vec{\mathbf{r}}_2 \ldots d\vec{\mathbf{r}}_N + \int \frac{Z_I}{|\vec{\mathbf{r}}_2 - \vec{\mathbf{R}}_I|} |\Psi(\vec{\mathbf{r}}_1, \ldots, \vec{\mathbf{r}}_N)|^2 d\vec{\mathbf{r}}_1 d\vec{\mathbf{r}}_2 \ldots d\vec{\mathbf{r}}_N + \ldots \Big]. \tag{2.27}$$

The Coulombic terms and wave function terms in the integrals can be separated:

$$V_{ne} = -\sum_{I=1}^{N_I}\Big[\int \frac{Z_I}{|\vec{\mathbf{r}}_1 - \vec{\mathbf{R}}_I|} d\vec{\mathbf{r}}_1 \int |\Psi(\vec{\mathbf{r}}_1, \ldots, \vec{\mathbf{r}}_N)|^2 d\vec{\mathbf{r}}_2 d\vec{\mathbf{r}}_3 \ldots d\vec{\mathbf{r}}_N + \int \frac{Z_I}{|\vec{\mathbf{r}}_2 - \vec{\mathbf{R}}_I|} d\vec{\mathbf{r}}_2 \int |\Psi(\vec{\mathbf{r}}_1, \ldots, \vec{\mathbf{r}}_N)|^2 d\vec{\mathbf{r}}_1 d\vec{\mathbf{r}}_3 \ldots d\vec{\mathbf{r}}_N + \ldots \Big]. \quad (2.28)$$

Since the second integral of each term is the density, $\rho(\vec{\mathbf{r}})$ as given in Eq. (2.11), V_{ne} can be expressed as:

$$V_{ne} = -\frac{1}{N_e}\sum_{I=1}^{N_I}\Big[\int \frac{Z_I}{|\vec{\mathbf{r}}_1 - \vec{\mathbf{R}}_I|} d\vec{\mathbf{r}}_1 \, \rho(\vec{\mathbf{r}}_1) + \int \frac{Z_I}{|\vec{\mathbf{r}}_2 - \vec{\mathbf{R}}_I|} d\vec{\mathbf{r}}_2 \, \rho(\vec{\mathbf{r}}_2) + \ldots \Big]. \quad (2.29)$$

When the equation is rearranged, the final form of the nuclei-electron potential energy can be written as:

$$V_{ne} = -\sum_{I=1}^{N_I} \int \rho(\vec{\mathbf{r}}) \, \frac{Z_I}{|\vec{\mathbf{r}} - \vec{\mathbf{R}}_I|} d\vec{\mathbf{r}} = \int \rho(\vec{\mathbf{r}}) \hat{V}_{ne}(\vec{\mathbf{r}}) d\vec{\mathbf{r}}. \quad (2.30)$$

If the three parts of the expectation value of the electronic Hamiltonian (Eq. (2.17), Eq. (2.25) and Eq. (2.30)) are summed up, the total ground state electronic energy is obtained:

$$E^{el} = T_{el} + V_{ee} + V_{ne} = -\frac{1}{2}\sum_{n}^{N_e} \int \phi_n^*(\vec{\mathbf{r}}) \nabla^2 \phi_n(\vec{\mathbf{r}}) d\vec{\mathbf{r}} + \Delta T_{el} + \frac{1}{2} \iint \frac{\rho(\vec{\mathbf{r}})\rho(\vec{\mathbf{r}'})}{|\vec{\mathbf{r}} - \vec{\mathbf{r}'}|} d\vec{\mathbf{r}} d\vec{\mathbf{r}'} + \Delta V_{ee} + \int \rho(\vec{\mathbf{r}}) \hat{V}_{ne}(\vec{\mathbf{r}}) d\vec{\mathbf{r}}. \quad (2.31)$$

All of the terms in the ground state electronic energy except the correction to the electronic kinetic energy term, ΔT_{el}, and the correction to the electron-electron potential energy term, ΔV_{ee}, are written in terms of density. The exchange-correlation energy is defined as the sum of these correction terms:

$$E_{xc} = \Delta T_{el} + \Delta V_{ee}. \quad (2.32)$$

2.3 The Hohenberg-Kohn Theorems

In 1964, Hohenberg and Kohn proposed two theorems [34] which are critical for establishing DFT as a legitimate quantum chemical methodology.

2.3.1 The Hohenberg-Kohn Existence Theorem

The first theorem of Hohenberg and Kohn shows that the electron density determines the Hamilton operator, $\hat{H}$, and therefore all properties of the system. The ground state density of a system in an external potential, $V_{ext}(\vec{\mathbf{r}})$, is uniquely determined by $V_{ext}(\vec{\mathbf{r}})$. This relation between the density and the external potential can be written as:

$$\rho(\vec{\mathbf{r}}) \Leftrightarrow V_{ext}(\vec{\mathbf{r}}). \tag{2.33}$$

The one-to-one mapping between the electron density $\rho(\vec{\mathbf{r}})$ and the external potential $V_{ext}(\vec{\mathbf{r}})$ can be easily proved. The mapping is:

$$V_{ext}(\vec{\mathbf{r}}) \xrightarrow{\text{Eq. (2.4)}} \Psi \xrightarrow{\text{Eq. (2.11)}} \rho(\vec{\mathbf{r}}). \tag{2.34}$$

2.3.2 Hohenberg-Kohn Variational Theorem

The first theorem is of considerable importance, however, it is not practical in providing any indication of how to calculate the density of a system. In a second theorem, Hohenberg and Kohn demonstrated that the density obeys the variational principle. Simply stated, the functional which gives the ground state energy of the system, delivers the lowest energy if and only if the density is the true ground state density, ρ_0.

For a well-behaved trial density $\rho(\vec{\mathbf{r}})$, which satisfies the necessary conditions such as $\rho(\vec{\mathbf{r}}) \geq 0$ and $\int \rho(\vec{\mathbf{r}}) d\vec{\mathbf{r}} = N$, the energy functional $E_{V_0}[\rho]$ of a system, in a particular external potential V_0 satisfies the relation:

$$E_{V_0}[\rho] \geq E_0 = E_{V_0}[\rho_0] \tag{2.35}$$

where E_0 is the ground state energy and ρ_0 is the ground state density. The proof of this inequality is very simple since it is very similar to the usual variational principle for wave functions. It should be recalled that any trial density, $\rho(\vec{\mathbf{r}})$, defines its own Hamiltonian, $\hat{H}$ and hence its own wave function, Ψ. The expectation value of this Hamiltonian generated from the true external potential V_{ext} with the trial wave function Ψ, which is not its ground state wave function Ψ_0, will never give an energy value lower than the true ground state energy:

$$\langle \Psi | \hat{H} | \Psi \rangle = T_{el}[\rho] + V_{ee}[\rho] + \int \rho(\vec{\mathbf{r}}) V_{ext} d\vec{\mathbf{r}} = E[\rho] \geq E_0[\rho_0] = \langle \Psi_0 | \hat{H} | \Psi_0 \rangle. \tag{2.36}$$

2.4 Non-Interacting Reference System

The second Hohenberg-Kohn theorem emphasized that the density determines the external potential which defines the Hamiltonian that determines the wave function. By using these Hamiltonian and wave function, the energy of the system can be computed. Nevertheless, if this direction is chosen, there would be no difference between DFT and other methods because the last step will be solving the Schrödinger equation. The clever solution to this problem was introduced by Kohn and Sham [35].

2.4.1 Kohn-Sham Equations

From the calculation of the electronic kinetic energy term in Eq. (2.15), it was seen that the difficulty was due to approximating the kinetic energy as a density functional. In 1965, Kohn and Sham [35] suggested that this difficulty can be overcome if only the kinetic energy expression:

$$T = -\frac{1}{2}\sum_{n}^{N_e}\int \phi_n^*(\vec{\mathbf{r}})\nabla^2\phi_n(\vec{\mathbf{r}})d\vec{\mathbf{r}} \tag{2.37}$$

is used to obtain the exact kinetic energy of the non-interacting reference system with the same density as the real, interacting one (it should be noted once again that since the density determines the position and atomic numbers of the nuclei, the density should be identical in the non-interacting and in the real systems):

$$T_{KS} = -\frac{1}{2}\sum_{i}^{N}\int \phi_i^*(\vec{\mathbf{r}})\nabla^2\phi_i(\vec{\mathbf{r}})d\vec{\mathbf{r}} \tag{2.38}$$

where ϕ_i represents the Kohn-Sham orbitals. It is clear that although the two systems share the same density, the non-interacting kinetic energy is not equal to the true kinetic energy of the interacting system, $T_{KS} \neq T$. Kohn and Sham also suggested that the difference between these terms can be appropriately approximated.

The energy functional can be divided into specific components:

$$E[\rho(\vec{\mathbf{r}})] = T_{KS}[\rho(\vec{\mathbf{r}})] + V_{ee}[\rho(\vec{\mathbf{r}})] + V_{ne}[\rho(\vec{\mathbf{r}})] + E_{xc}[\rho(\vec{\mathbf{r}})]. \tag{2.39}$$

By using the Kohn-Sham expression for the density, Eq. (2.38), the total electronic energy in

Eq. (2.39) can be written as:

$$E[\rho(\vec{\mathbf{r}})] = -\frac{1}{2}\sum_{i}^{N}\int \phi_i|\nabla^2|\phi_i + \frac{1}{2}\sum_{i}^{N_e}\sum_{j\neq i}^{N_e}\iint |\phi_i(\vec{\mathbf{r}})|^2\frac{1}{|\vec{\mathbf{r}}-\vec{\mathbf{r}'}|}|\phi_j(\vec{\mathbf{r}'})|^2 d\vec{\mathbf{r}}d\vec{\mathbf{r}'} - \sum_{I}^{N_n}\int\sum_{i}^{N_e}\frac{Z_I}{|\vec{\mathbf{r}}-\vec{\mathbf{R}}_I|}|\phi_i(\vec{\mathbf{r}})|^2 d\vec{\mathbf{r}} + E_{xc}[\rho(\vec{\mathbf{r}})]. \quad (2.40)$$

In this equation, the only term that does not have an explicit form is the exchange-correlation functional, $E_{xc}[\rho(\vec{\mathbf{r}})]$. The Kohn-Sham orbitals, ϕ_i, are taken to fulfill the condition to minimize the energy expression above while remaining mutually orthonormal. They satisfy the Kohn-Sham equation

$$\hat{H}_{KS}\phi_i = \epsilon_i\phi_i \quad (2.41)$$

where the Kohn-Sham single-electron operator, $\hat{H}_{KS}$, is defined as

$$\hat{H}_{KS} = -\frac{1}{2}\nabla^2 + \int\frac{\rho(\vec{\mathbf{r}'})}{|\vec{\mathbf{r}}-\vec{\mathbf{r}'}|}d\vec{\mathbf{r}'} - \sum_{I}^{N_n}\frac{Z_I}{|\vec{\mathbf{r}}-\vec{\mathbf{R}}_I|} + \hat{V}_{xc}(\vec{\mathbf{r}}) = \left(-\frac{1}{2}\nabla^2 + \hat{V}_{eff}(\vec{\mathbf{r}})\right) \quad (2.42)$$

where $\hat{V}_{xc}$ is the potential due to exchange-correlation energy, E_{xc} and is given by the functional derivative of E_{xc} with respect to ρ;

$$\hat{V}_{xc} = \frac{\delta E_{xc}}{\delta\rho}. \quad (2.43)$$

The $\hat{V}_{eff}$ term is the effective potential operator is then

$$\hat{V}_{eff} = \left[\int\frac{\rho(\vec{\mathbf{r}'})}{|\vec{\mathbf{r}}-\vec{\mathbf{r}'}|}d\vec{\mathbf{r}'} - \sum_{I}^{N_n}\frac{Z_I}{|\vec{\mathbf{r}}-\vec{\mathbf{R}}_I|} + \hat{V}_{xc}(\vec{\mathbf{r}})\right]. \quad (2.44)$$

It should be noted that the Kohn-Sham equations depend directly on the density and indirectly on the orbitals since $\hat{V}_{eff}$ depends on the density and orbitals through the Coulomb term as shown in Eq. (2.40). If there is a change in the Kohn-Sham orbitals, then the potential will also change. For this reason, the Kohn-Sham one-electron equations (Eq. (2.41)) have to be solved self-consistently from an initial guess for the electron density, $\rho(\vec{\mathbf{r}})$.

2.4.2 Exchange-Correlation Functionals

An explicit form of the unknown functional for the exchange-correlation energy, $E_{xc}[\rho(\vec{\mathbf{r}})]$, is needed for a practical solution of the Kohn-Sham equations and thus the central goal of modern density functional theory is to find better approximations for this term. One popular

approximation to $E_{xc}[\rho(\vec{\mathbf{r}})]$ is the local density approximation (LDA) whose general idea is to take the known result of a homogeneous electron gas system and to apply it locally to a non-uniform system. The exchange-correlation energy in LDA is written as:

$$E_{xc}^{LDA}[\rho] = \int \rho(\vec{\mathbf{r}})\epsilon_{xc}(\rho(\vec{\mathbf{r}}))d\vec{\mathbf{r}} \tag{2.45}$$

where $E_{xc}(\rho(\vec{\mathbf{r}}))$ is the exchange-correlation energy per particle of a uniform electron gas of $\rho(\vec{\mathbf{r}})$.

The exchange-correlation potential can be obtained as:

$$\hat{V}_{xc}^{LDA}(\vec{\mathbf{r}}) = \frac{\delta E_{xc}^{LDA}[\rho]}{\delta\rho(\vec{\mathbf{r}})} = E_{xc}(\rho(\vec{\mathbf{r}})) + \rho(\vec{\mathbf{r}})\frac{\partial E_{xc}}{\partial\rho} \tag{2.46}$$

and the Kohn-Sham equation can be written as

$$\hat{H}_{KS}^{LDA}\phi_i(\vec{\mathbf{r}}) = \left[-\frac{1}{2}\nabla^2 + \int \frac{\rho(\vec{\mathbf{r}'})}{|\vec{\mathbf{r}} - \vec{\mathbf{r}'}|}d\vec{\mathbf{r}'} - \sum_I^{N_n} \frac{Z_I}{|\vec{\mathbf{r}} - \vec{\mathbf{R}}_I|} + \hat{V}_{xc}^{LDA}(\vec{\mathbf{r}})\right]\phi_i(\vec{\mathbf{r}}) = \epsilon_i\phi_i(\vec{\mathbf{r}}). \tag{2.47}$$

It is clear that in this approximation the exchange-correlation energy depends only on the density. In spite of this considerably simple approach, LDA gives good results for bulk properties. Nevertheless, it is inadequate for molecular systems in which the charge density is non-uniform where $E_{xc}[\rho(\vec{\mathbf{r}})]$ depends also on the gradient of the density.

The second popular approximation to the $E_{xc}[\rho]$ is the generalized gradient approximation (GGA) whose accuracy is beyond LDA for inhomogeneous systems because the dependence on the gradient of the density is included in the exchange-correlation energy per particle of a weakly inhomogeneous electron gas [36]:

$$E_{xc}^{GGA}[\rho] = \int \rho(\vec{\mathbf{r}})E_{xc}[\rho(\vec{\mathbf{r}}), \nabla\rho(\vec{\mathbf{r}})]d\vec{\mathbf{r}}. \tag{2.48}$$

The most popular GGA types are PBE (Perdew, Burke and Ernzerhof) [36] and BLYP (Becke, Lee, Yang and Parr) [37, 38]. The PBE functional is recommended for the bulk calculations and molecules interacting with the metallic surfaces. For this reason, the PBE functional has been used in our calculations.

2.5 Basis Set Expansion of the Kohn-Sham Orbitals

Density Functional Theory, in the Kohn-Sham approach, replaces the interacting many-particle system by an auxiliary system of non-interacting particles. The connection between this artificial system and the real one is provided by choosing the V_{eff} in a way that the density

resulting from the sum of the absolute square of these orbitals is equal to the density of the real system of interacting particles. The Hamiltonian of this artificial non-interacting system is obtained self-consistently. However, the Kohn-Sham equations (Eq. (2.41) and Eq. (2.42)) are extremely complicated and are difficult to solve in real space.

In order to solve the Kohn-Sham equations, one needs to develop strategies for facilitating the iterative self-consistent field procedure. An applicable strategy is to expand the Kohn-Sham orbitals, ϕ_i, in a suitable basis. Eq. (2.41) is therefore converted into a matrix eigenvalue equation. For periodic systems, the most convenient choice of basis set is plane-waves. The Kohn-Sham orbitals can be expanded in terms of plane-waves as

$$\phi_i(\vec{\mathbf{r}}) = \frac{1}{\sqrt{\Omega}} \sum_{\vec{q}} c_{i,\vec{q}} \exp(i\vec{q} \,.\, \vec{\mathbf{r}}) \equiv \sum_{\vec{q}} c_{i,\vec{q}} |\vec{q}\rangle \tag{2.49}$$

where $c_{i,\vec{q}}$ is the expansion coefficient and Ω is the volume of the crystal.

By introducing the above equation in Eq. (2.41), multiplying it by $\langle\vec{q'}|$ from the left and then integrating, a matrix eigenvalue equation is obtained:

$$\sum_{\vec{q}} c_{i,\vec{q}} \langle\vec{q'}|\hat{H}_{KS}|\vec{q}\rangle = \epsilon_i \sum_{\vec{q}} c_{i,\vec{q}} \langle\vec{q'}|\vec{q}\rangle = \epsilon_i c_{i,\vec{q}}. \tag{2.50}$$

This matrix equation can be written as

$$\bar{H}C = \epsilon_i C \tag{2.51}$$

where $\bar{H}$ is the matrix representation of the Hamiltonian in the plane-wave basis and C is the vector of coefficients. For simplification, operators forming the Hamiltonian should be considered separately. The kinetic energy term can be written in the plane-wave basis as

$$\langle\vec{q'}| -\frac{1}{2}\nabla^2 |\vec{q}\rangle = \frac{1}{2}|\vec{q}|^2 \delta_{\vec{q}\vec{q'}}. \tag{2.52}$$

The effective potential energy term of the Kohn-Sham single-electron operator, $\hat{H}_{KS}$, is periodic and Fourier transform can be used to express this term in matrix form. The effective potential, V_{eff}, has the periodicity of the unit cell and for this reason only terms with the wavevectors ($\vec{G}$) in the reciprocal space of the periodic system will be allowed:

$$\hat{V}_{eff}(\vec{\mathbf{r}}) = \sum_{m} \hat{V}_{eff}(\vec{G}_m) \exp(i\vec{G}_m \,.\, \vec{\mathbf{r}}). \tag{2.53}$$

The Fourier transform from real space to reciprocal space is

$$\hat{V}_{eff}(\vec{G}) = \frac{1}{\Omega_{cell}} \int_{\Omega_{cell}} \hat{V}_{eff}(\vec{\mathbf{r}}) \exp(-i\vec{G}_m \,.\, \vec{\mathbf{r}}) d\vec{\mathbf{r}}. \tag{2.54}$$

The matrix elements of the effective potential can be calculated by inserting V_{eff} into Eq. (2.51) as:

$$\langle\vec{q'}|\hat{V}_{eff}|\vec{q}\rangle = \sum_m \langle\vec{q'}|\hat{V}_{eff}(\vec{G}_m)|\vec{q}\rangle \exp(i\vec{G}_m \,.\, \vec{\mathbf{r}}) \equiv \sum_m \langle\vec{q'}|\hat{V}_{eff}(\vec{G}_m)|\vec{q}+\vec{G}_m\rangle$$
$$= \sum_m V_{eff}(\vec{G}_m)\langle\vec{q'}|\vec{q}+\vec{G}_m\rangle = \sum_m V_{eff}(\vec{G}_m)\delta_{\vec{q'}-\vec{q},\vec{G}_m}. \quad (2.55)$$

In Eq. (2.55), only the terms with the wavevectors that differ by a reciprocal lattice vector give nonzero contributions. For the representation in terms of $\vec{G}_m$, the new definitions; $\vec{q} = \vec{k} + \vec{G}_m$ and $\vec{q'} = \vec{k} + \vec{G}_{m'}$ will be used. Eq. (2.51) can be written as:

$$\sum_m \Big[\frac{1}{2}|\vec{k}+\vec{G}_m|^2\delta_{m,m'} + V_{eff}(\vec{G_m} - \vec{G_{m'}})\Big]c_{i,\vec{k}+\vec{G}} = \epsilon_i c_{i,m'}. \quad (2.56)$$

In order to point out the $\vec{k}$-dependence of Eq. (2.56) in accord with Bloch's theorem, it can be rewritten as:

$$\sum_m \hat{H}_{m,m'}(\vec{k})c_{i,m}(\vec{k}) = \epsilon_i(\vec{k})c_{i,m'}(\vec{k}). \quad (2.57)$$

Eq. (2.56) and Eq. (2.57) are matrix equations in which the effective potential term depends on the difference between two reciprocal lattice vectors. V_{eff} contains the Hartree potential term, the exchange-correlation potential term and the external potential term.

The density can also be written in terms of plane-waves. Eq. (2.16) represents the electron density in real space and Eq. (2.49) is the expansion of the Kohn-Sham orbitals in terms of plane-waves. If the latter is inserted in Eq. (2.16), then the density can be written as:

$$\rho_{i,\vec{k}} = \frac{1}{\Omega}\sum_m\sum_{m'} c^*_{i,m}(\vec{k})\exp(i(\vec{G}_{m'} - \vec{G}).\vec{r})c_{i,m'}(\vec{k}). \quad (2.58)$$

Eq. (2.58) can be simplified as:

$$\rho_{i,\vec{k}}(\vec{G}) = \frac{1}{\Omega}\sum_m c^*_{i,m}(\vec{k})c_{i,m''}(\vec{k}) \quad (2.59)$$

where m'' is the index of the vector $\vec{G}_{m''} = \vec{G} + \vec{G}_m$. All the terms in the above equation are written in terms plane-waves, however, the expansion in terms of plane-waves must be truncated for computational cost. In DFT calculations there is a parameter which determines the energy cut-off. This parameter enables the DFT codes to use only the plane-waves which satisfy:

$$\frac{1}{2}|\vec{G}|^2 < E_{cut}. \quad (2.60)$$

In order to choose the proper energy cut-off parameter, convergence studies must be performed.

2.6 The Pseudopotentials

The plane-wave basis is appropriate for the expansion of the Kohn-Sham orbitals due to the simplicity of the integrals to be evaluated and the convenience that this basis set can be enlarged systematically by using a single parameter, the kinetic energy cut-off, E_{cut}. Unfortunately, using plane-wave basis set to describe all electrons of a system would be impractical since a huge number of plane-waves is required for the accurate representation of the rapidly oscillating electronic wave functions in the core region. A practical solution is given by the use of pseudopotentials.

Before explaining the key points of the pseudopotentials, the distinction between the valence and core electrons should be made. It is known that the valence electrons are responsible for the chemical properties of a material, whereas the core electrons are usually inert. Even though these core electrons do not get involved in chemical interactions, there are two pivotal effects of the core electrons on the valence electrons. The first one is that the core orbitals make contribution to the Hartree and exchange-correlation potentials which are felt by the valence electrons. The second one is that since the electronic wave function of the core electrons has a highly oscillatory behavior in the field of the nuclei, on account of the orthogonality condition, the wave function of the valence electrons also display an oscillatory behavior in this region.

There are three options to solve this problem. The first one is to compute the core orbitals self-consistently in an all-electron (AE) calculation. The next one is counting the core orbitals as a part of the electron density, however considering them as frozen during the minimization of the total energy. This method is called the frozen-core approximation. The last option is far more radical than the others and it is widely used. It is replacing the oscillatory core part by smoother pseudowavefunctions for saving computational effort.

To sum up the pseudopotential approach, one may begin with the fact that the expansion of rapidly oscillating wave functions in terms of plane-waves is very complicated. For this reason, all-electron wave function, $\phi^{(AE)}$, is replaced by a smoother and nodeless wave function,

$\phi^{(PS)}$, as illustrated in Figure 2.1.

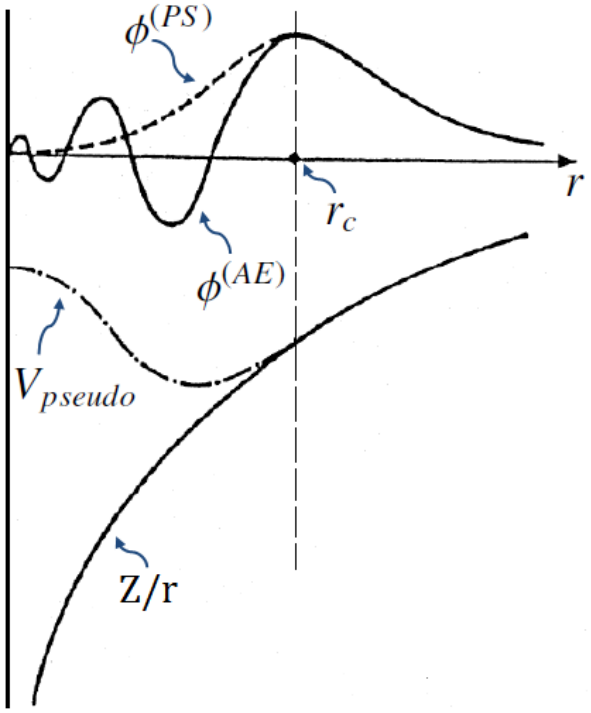

Figure 2.1: Schematic representation of the all-electron (AE) wave function, all-electron potential (Z/r), the pseudowavefunctions and the pseudopotentials.

There are certain criteria that a pseudopotential has to obey. The first one is that the eigenvalues of the all-electron wave function and pseudowavefunction have to be conserved [39]:

$$\hat{H}\,|\phi_i^{(AE)}\rangle = \epsilon_i\,|\phi_i^{(AE)}\rangle \tag{2.61}$$

$$(\hat{H} + \hat{V}_{pseudo})\,|\phi_i^{(PS)}\rangle = \epsilon_i\,|\phi_i^{(PS)}\rangle. \tag{2.62}$$

The next criterion is that the pseudowavefunctions and the all-electron wave functions need to coincide outside the core region ($r > r_c$):

$$\phi_i^{(AE)}(r) = \phi_i^{(PS)}(r) \tag{2.63}$$

as shown in the Figure 2.1. The third requirement is that the integration of the norm squares of these wave functions have to be equal inside the cut-off radius, r_c:

$$\int_0^{r_c} |\phi^{(AE)}(r)|^2 dr = \int_0^{r_c} |\phi^{(PS)}(r)|^2 dr. \tag{2.64}$$

This condition is called the *norm-conservation* and the physical meaning of this requirement is that the number of the electrons (total charge) inside the radius r_c is properly given by the

pseudowavefunction. This kind of pseudopotential is referred to as *norm-conserving* pseudopotential [40].

The last criterion is that the scattering properties of the all-electron potential have to be conserved:

$$\left[\frac{d}{dr}\, ln(\phi^{(AE)}(r))\right]_R = \left[\frac{d}{dr}\, ln(\phi^{(PS)}(r))\right]_R \tag{2.65}$$

where the $R < r_c$ [39].

Many modern pseudopotentials produce much smoother (softer) pseudowavefunctions and use fewer plane-waves for calculations to save computational effort [41]. These pseudopotentials were developed by Vanderbilt [41] and are called *ultrasoft* pseudopotentials. This development is satisfied by dropping the norm-conservation condition and using compensating terms (augmented electron density) to provide the true electron density, and adding reference energies to improve the scattering properties of the pseudopotential. Relaxing the norm-conserving constraint gives more flexibility for generating the pseudowavefunctions. In our calculation Vanderbilt type ultrasoft pseudopotentials were used.

2.7 DFT Implementation in the Quantum-Espresso Code

The calculations in this thesis were performed by using the Quantum-Espresso (QE) package [42], which employs the Plane-Wave-Self-Consistent field (PWscf) approach. QE is an open source code based on density functional theory, plane-waves, and pseudopotentials. Various structural, electronic and cohesive properties of atoms, molecules and solids can be calculated by using Quantum-Espresso.

The surfaces are represented by three dimensional periodically repeated unit cells. The Kohn-Sham orbitals are expanded in terms of plane-waves and the core electrons are represented by an effective potential. By using the local density approximation (LDA) or general gradient approximation (GGA), the contribution of the exchange-correlation energy to the total energy is implemented.

Many efficient algorithms have been developed for the solution of the SCF procedure. In this study we use the Davidson algorithm for the matrix diagonalization.

2.7.1 Structure Relaxation

The geometry optimization is carried out on a single unit cell which is periodically repeated in three dimensions. In order to prevent the interaction between the adsorbate and the subsequent slab, the vacuum thickness needs to be large enough. Moreover, the lateral size of the unit cell is crucial to avoid the interaction between two adsorbates. For this reason, p(2 x 1) or p(2 x 2) unit cells and a vacuum thickness between 11-12 Å are used in all calculations in this thesis. The slab also needs to be thick enough to serve as a complete representation of both the bulk and the surface atoms. Such a system is illustrated in the Figure 2.2. The structure optimization enables the system to reach the most stable geometry in conjunction with the minimum energy.

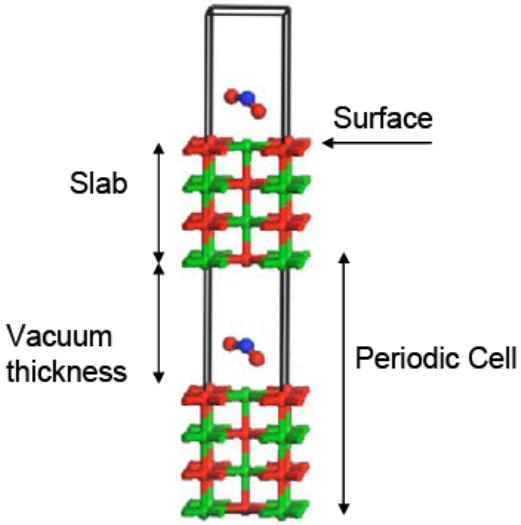

Figure 2.2: Representation of a p(1 x 1) unit cell with a slab consisting of four layers. The vacuum is in the z-direction.

2.7.2 Calculation of Adsorption Energy

The adsorption energy of a system, E_{ads}, is defined as the difference between the total energy of the slab with the adsorbate, $E_{slab+adsorbate}$, and the sum of the total energies of the clean surface, E_{slab}, and the free adsorbate, $E_{adsorbate}$, [19, 28]:

$$E_{ads} = E_{slab+adsorbate} - (E_{slab} + E_{adsorbate}). \tag{2.66}$$

With this convention, negative adsorption energy indicates exothermic adsorption [19]. The higher the absolute value of the adsorption energy is, the stronger the interaction between the adsorbate and the surface is.

2.7.3 DOS and PDOS Calculations

Density of states (DOS) is the total number of the states in any given interval and describes the states in the bands and their dependence on energy. The DOS calculations enable one to obtain discrete energy states with elevated resolution and these calculations start with a self-consistent calculation to acquire the wave function. In the case of the partial density of states (PDOS) calculations, generating the PDOS necessitates the projection of the Kohn-Sham eigenstates onto a suitably defined atomic region. The PDOS calculation is a useful tool for analyzing the charge transfer in a chemical process. In this thesis, the charge transfer analysis was done by PDOS calculations.

CHAPTER 3

RESULTS AND DISCUSSION

In this chapter, the (100) surface of BaO with dopants (K, Na, Ca and La), (100) and (110) surfaces of Li_2O, Na_2O and K_2O are investigated as storage materials and alkali metal (Li, Na and K) loaded (001) surface of TiO_2 (titania) anatase is investigated as a support material for the NO_x storage and reduction catalysts. The results are compared with results obtained for the bare (100) BaO and (001) TiO_2 surfaces.

The calculations are done using the Quantum-Espresso package. For the exchange-correlation functional, the Perdew-Burke-Ernzerhof (PBE) approximation [36] is used. The interaction of the valence electrons with the atomic core states is described by ultrasoft pseudopotentials.

Barium oxide containing NSR catalysts are active for the abatement of NO_x from the exhaust of the lean-burn engines [19, 20] and BaO is therefore widely studied as the storage material of these catalysts. Unfortunately, the SO_x tolerance of barium oxide is very low. In order to decrease the sulfur poisoning effects, the impact of dopants on the NO_x storage performance of BaO is investigated.

The stability of the adsorbate is determined by the basicity of the adsorbent. Highly basic storage materials show low SO_x tolerance [13, 15]. Alkali metal oxides Li_2O through K_2O were chosen as the storage component and the effect of the basicity of the storage material on sulfur poisoning is investigated.

Support material not only supplies high surface area, but also provides additional storage sites for NO_x and increases sulfur durability. The importance of the support material for increasing the SO_x tolerance is proven by the results of the combined use of TiO_2 and γ-Al_2O_3 [43]. Even though γ-Al_2O_3 is the most extensively used support component of the NSR catalysts,

titania has higher sulfur durability than alumina [32]. Unfortunately, the NO_x storage capacity of the TiO_2 is low. In order to increase the SO_x tolerance while retaining an acceptable NO_x storage capacity, alkali metal (Li, Na and K) loaded TiO_2 surfaces are studied.

3.1 Preliminary Calculations

For testing the accuracy of the parameters that are used in our calculations, bulk calculations were performed to determine the lattice constant of BaO, Li_2O, Na_2O, K_2O and TiO_2.

The determination of the lattice constant is also a test for the accuracy of the pseudopotentials that are used in the calculations. If the calculated lattice parameters are in agreement with the experimental values within an acceptable error range (1%), then the chosen pseudopotentials can be safely employed in subsequent calculations.The lattice constant calculations of bulk CaO, La_2O_3, Li, Na and K were also performed.

3.1.1 Bulk Structure of BaO

Barium oxide is a crystalline solid and has the rock salt structure as shown in Figure 3.1.

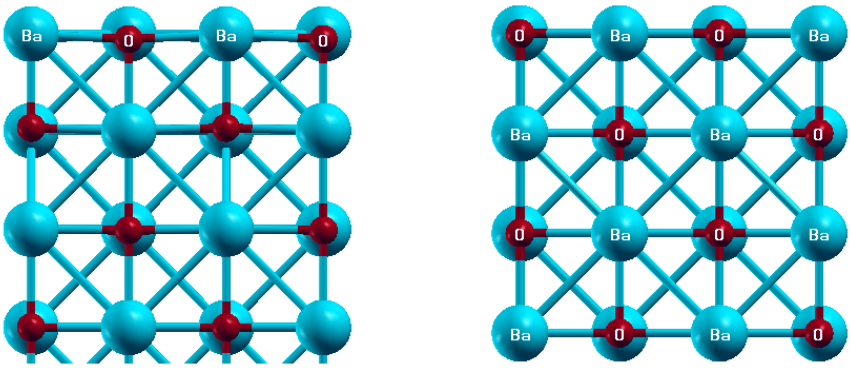

Figure 3.1: Side and top views of surface atoms of the BaO bulk structure.

The computed lattice constant (5.582 Å) is in good agreement with the experimental (5.523 Å [44]) and previous theoretical (5.608 Å [45]) values. Convergence of the computed lattice parameters is checked by increasing the kinetic energy cut-off and the number of the k-points.

This preliminary study revealed that a kinetic energy cut-off of 40 Ryd, an augmented electron density cut-off of 400 Ryd and a 3x3x1 k-points mesh give reasonably accurate results.

3.1.2 Bulk Structure of Li_2O, Na_2O and K_2O

The alkali metal oxides crystallize in the cubic antifluorite (anti-CaF_2) structure in which the cations (alkali metal atoms) form a simple cubic lattice and the anions (oxygen atoms) form an fcc lattice. The coordination geometry of these oxides is tetrahedral for the metal cation and cubic for the oxygen anion. Each metal cation is coordinated with four oxygen anions and each oxygen anion is surrounded by eight metal cations as illustrated in Figure 3.2. Exactly the same procedure that is used for the lattice constant calculation of BaO is followed.

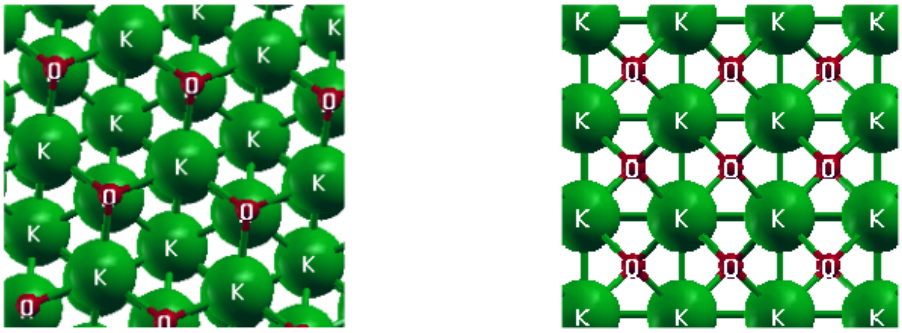

Figure 3.2: Side and top views of the K_2O bulk structure.

The results obtained for Li_2O, Na_2O and K_2O are summarized in Table 3.1. These theoretical lattice constants agree well with experimental [46] and previous calculations [47]. It is clear that the results do not change appreciably with varying kinetic energy cut-off and therefore 30 Ryd was chosen as E_{cut} for the present calculations.

Table 3.1: Calculated lattice constants (Calc.) of alkali metal oxides in Å. The experimental (Exp.) [46] and theoretical (Theo.) values from literature [47] are included. The errors with respect to the experimental values are indicated as percentage in parentheses.

	E_{cut} [Ryd]	Li_2O	Na_2O	K_2O
Calc.	30	4.645 (0.56%)	5.598 (0.68%)	6.488 (0.60%)
Calc.	40	4.642 (0.50%)	5.597 (0.67%)	6.485 (0.56%)
Exp. [46]	-	4.619	5.560	6.449
Theo. [47]	-	4.58	5.47	6.42

A convergence study with respect to k-point sampling was done and 6x6x1, 8x8x1, and 4x4x1 mesh of k-points were found adequate for the bulk of Li_2O, Na_2O and K_2O, respectively.

3.1.3 Lattice constant calculations of CaO and La_2O_3

The impact of the dopants on the NO_x storage and reduction performance of NSR catalysts including BaO was investigated. The introduced dopants were chosen with the aim of examining the impacts of the different lattice spacing, the increased and decreased oxidation state of the metal atoms of the storage material. For this reason, Ca and La doped BaO (100) surfaces were also investigated. For testing the compatibility of the corresponding pseudopotentials, lattice constant calculations of CaO and La_2O_3 were performed as well.

Calcium oxide also has rock salt structure like barium oxide and its lattice parameter is obtained using the same procedure as the one used for BaO. The calculated equilibrium lattice constant of calcium oxide (4.836 Å) is in agreement with the experimental (4.811 Å [44]) and previous theoretical (4.832 Å [45]) values.

La_2O_3 is an A-type sesquioxide and crystallizes in the hexagonal space group $P\bar{3}m1$ ($a = b \neq c$, α=β=90° and γ=120°). The lanthanum atoms are surrounded by the oxygen atoms (anions) which are arranged in an octahedral geometry around the cations as illustrated in Figure 3.3. The fixed volume and the variable-cell relaxation studies are undertaken to calculate the lattice constants of bulk structure of lanthanum(III) oxide. The optimized cell parameters (a=3.895 Å, c=6.083 Å) are in good agreement with the reported experimental (a=3.939 Å, c=6.136 Å [48]) and theoretical (a=3.95 Å, c=6.15 Å [48]) values.

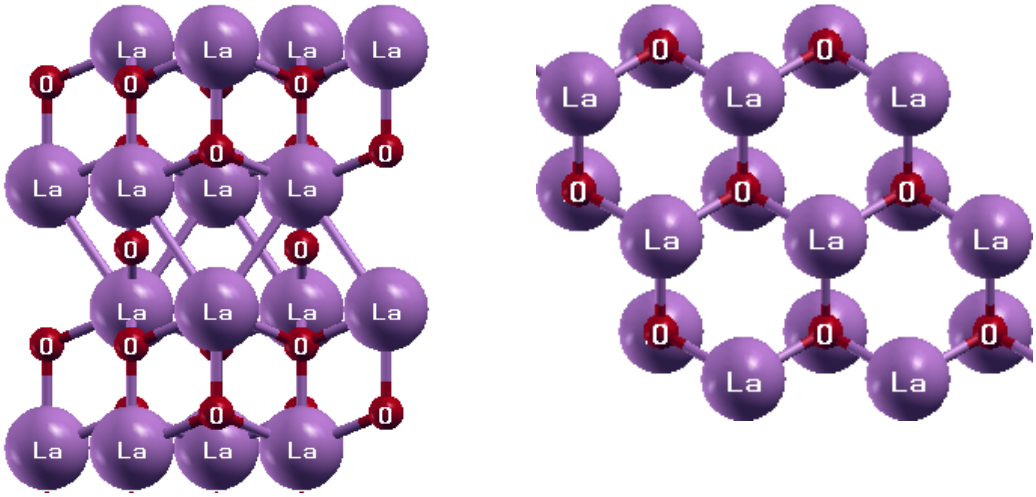

Figure 3.3: Side and top views of La_2O_3 bulk structure.

3.1.4 Bulk Calculations of TiO_2, Li, Na and K

Titanium dioxide, also known as titanium(IV) oxide or titania, has three well-known polymorphs: rutile, anatase and brookite. Rutile is the most stable and brookite is the least stable of them. Although rutile is more stable than anatase, the surface properties of the anatase are more desirable and it is therefore studied frequently [49]. TiO_2 anatase belongs to tetragonal crystal system ($a = b \neq c$, α=β=γ=90°, Figure 3.4).

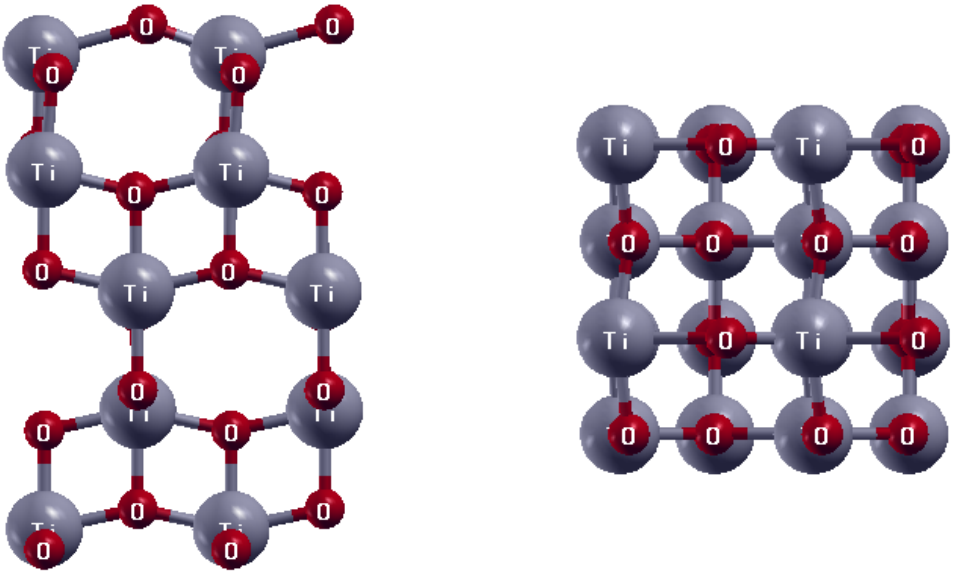

Figure 3.4: Side and top views of TiO_2 anatase structure

For the lattice constants of anatase TiO_2, the results of a former study in our group were used. Computed cell parameters (a=3.786 Å, c=9.619 Å [50]) are in good agreement with experimental (a=3.782 Å, c=9.502 Å [51]) and published theoretical (a=3.786 Å, c=9.737 Å [49]) values.

The crystal structure of lithium, sodium and potassium is body-centered cubic (space group of Im3m). In order to test the accuracy of the pseudopotentials, lattice constant calculations of Li, Na and K were carried out and the results are reported in Table 3.2. These values are in agreement with the experimental values [52].

Table 3.2: Calculated lattice constants (Calc.) of bulk structure of alkali metals in Å. The errors with respect to the experimental values (Exp.) [52] are shown as percentage in parentheses.

	E_{cut} [Ryd]	Li	Na	K
Calc.	30	3.557 (1.37%)	4.256 (0.82%)	5.282 (0.73%)
Calc.	40	3.555 (1.31%)	4.259 (0.75%)	5.283 (0.71%)
Exp. [52]	-	3.509	4.291	5.321

3.1.5 Gas Phase Species

The equilibrium geometries of the gas phase adsorbates were determined by performing an unconstrained geometry optimization. The geometric parameters of these gas phase molecules were calculated in a 16 Å cubic cell with kinetic energy cut-off and the augmented electron density cut-off set to 40 Ryd and 400 Ryd, respectively.

The results are summarized in Table 3.3. The calculated bond lengths and angles agree within 1% with reported theoretical [21, 27] and experimental [53] values.

Table 3.3: Comparison of the calculated parameters with the reported theoretically and experimentally obtained values. d is the bond length and θ is the bond angle.

	This Work		Theo. [21, 27]		Exp. [53]	
	d [Å]	θ [°]	d [Å]	θ [°]	d [Å]	θ [°]
NO_2	1.212	133.5	1.213	133.4	1.20	134.1
SO_2	1.459	119.3	1.454	119.5	1.43	119.5

3.2 Surface Calculations

The development and increasing scope of applications of catalysts in industrial processes stimulate a better knowledge of their physico-chemical properties. The surface energy belongs to these properties since it is a parameter that indicates the character of the interfacial phenomena (e.g. adsorption, wetting, adhesion, etc).

The interaction between matter and its surroundings occurs through the surface and the stability of a surface is correlated to its cell parameters. Since periodicity is crucial for plane wave-based DFT software, surfaces are generated by infinitely many periodically repetitive slabs with starting atomic coordinates obtained from the bulk structure. Therefore, the system needs to be separated by a large enough vacuum, which prevents the interaction between the periodic images.

The surface energy of a unrelaxed or fully-relaxed slab is defined as the difference between the total energy of the slab and the total energy of an equal number of atoms in the bulk divided by twice the surface area [49]:

$$E_{surf} = \frac{E_{slab} - (\frac{N_{slab}}{N_{bulk}})E_{bulk}}{2Area} \tag{3.1}$$

In order to describe bulk to surface transition in a realistic way, some of the bottom layers of the slab need to be fixed. This kind of slabs (partially fixed slabs) are asymmetric systems since reconstruction takes place due to the relaxation. As a result, the surface energy of an asymmetric slab is described as the difference between the formation energy of the partially fixed slab and the surface energy of the unrelaxed slab [49, 54]:

$$E_{surf-fixed} = \frac{E_{slab} - (\frac{N_{slab}}{N_{bulk}})E_{bulk}}{Area} - E_{surf(unrelax)} \tag{3.2}$$

The interaction between the periodically repeated slabs is prevented by a vacuum thickness of approximately 11-12 Å between these slabs and larger values for the vacuum are used to check for dipole interaction.

3.2.1 (100) Surface of Barium Oxide

Four layer slabs with the bottom two layers fixed are considered to be thick enough to represent both the bulk and the surface atoms. Thus, four layer slabs are used in the rest of the thesis to minimize the computational costs. In order to test the accuracy of the k-point sampling, surface energies with 3x3x1 and 4x4x1 k-points meshes are calculated. Two different kinetic energy cut-off (E_{cut}) values and smearing types are used. The results are summarized in Table 3.4 and they are in good agreement with the previous theoretical values (0.35 [45] and 0.4 [20, 55]). It can be concluded that a 3x3x1 k-points mesh is suitable for our calculations.

Table 3.4: Surface energies of (100) BaO surface for a four-layer slabs in J/m^2. Kinetic energy cut-off is in Ryd.

k-point	Smearing	E_{cut}	Layer/fixed	E_{surf}	E_{cut}	Layer/fixed	E_{surf}
3x3x1	Gaussian	30	4/0	0.325	40	4/0	0.326
3x3x1	Gaussian	30	4/2	0.399	40	4/2	0.399
3x3x1	Gaussian	30	4/4	0.399	40	4/4	0.399
3x3x1	MV	30	4/0	0.339	40	4/0	0.339
3x3x1	MV	30	4/2	0.396	40	4/2	0.397
3x3x1	MV	30	4/4	0.396	40	4/4	0.397
4x4x1	Gaussian	30	4/0	0.325	40	4/0	0.325
4x4x1	Gaussian	30	4/2	0.398	40	4/2	0.399
4x4x1	Gaussian	30	4/4	0.399	40	4/4	0.399
4x4x1	MV	30	4/0	0.338	40	4/0	0.339
4x4x1	MV	30	4/2	0.391	40	4/2	0.391
4x4x1	MV	30	4/4	0.401	40	4/4	0.402

By looking at the small differences between the results, it can be concluded that a four layer model is adequate to represent the BaO (100) surface and fixing two layers is appropriate for making the complete representation of the bulk in the slab. The slight underestimation of the surface energy and overestimation of the lattice constant is common for the Perdew-Burke-Ernzerhof exchange-correlation functional [20]. For metallic systems, there are variables that are used for specifying how the metallic system should be treated. One of these variables is smearing which expands the occupations of the Kohn-Sham states by a slowly changing function. Gaussian, Marzari-Vanderbilt (MV), Methfessel-Paxton (MP) and Fermi-Dirac (FD) are types of smearing. Surface energy calculations were also aimed to test the reliability of the type of the smearing chosen. The results of these calculations revealed that the Gaussian

type smearing is more adequate than the MV type smearing and therefore the Gaussian type smearing is used in all of our calculations.

3.2.2 (100) and (110) Surfaces of Li_2O, Na_2O and K_2O

Even though (100) surface is the most stable surface of alkali metal oxides, it is not a stoichiometric surface and for this reason, the surface energy cannot be easily calculated. After using (100) surfaces to test the expediency of these oxides as a storage material and concluding that these oxides are adequate for the abatement of NO_x, the stoichiometric surfaces (110) of these oxides were generated and surface energy calculations were performed. There are 60 atoms in the unit cell which contains five layer slabs with the bottom two layers fixed. These supercells are thought to be a good representation of the bulk and the surface atoms which is proven by the results of the surface energy calculations presented in the Table 3.5. The surface energies of the four, five and six layer slabs were calculated. Due to the computational cost, surface energy calculations were only done for the Li_2O. The results are reported in the Table 3.5.

Table 3.5: Surface energies of Li_2O (110) surface for five layer slab in J/m^2. The results of a former study [56] are in parenthesis.

Layer/fixed	E_{surf}	Layer/fixed	E_{surf}	Layer/fixed	E_{surf}
4/0	0.981 (1.410)	5/0	1.167 (1.410)	6/0	1.172 (1.410)
4/2	1.269 (1.410)	5/2	1.432 (1.410)	6/2	1.437 (1.410)
4/4	1.641 (1.630)	5/5	1.688 (1.630)	6/6	1.690 (1.640)

3.3 NO_2 and SO_2 Adsorptions

As stated before the exhaust gas contains NO and NO_2, however NO generally gets oxidized and forms NO_2 in the presence of oxygen during the lean phase (excess oxygen condition):

$$NO \xrightarrow[Pt]{O_2} NO_2. \tag{3.3}$$

Therefore, only the adsorption of the NO_2 is considered in this study. Furthermore, only the adsorption of the SO_2 molecule is being considered.

A large number of periodic supercell [20, 28, 55] and cluster model [21-23, 25-27] calculations based on ab-initio quantum chemistry methods have previously been performed to

investigate the interaction between the NO_x and barium oxide surfaces. As following the same trend, we begin our study with an investigation of the adsorption geometries and binding pattern of the NO_2 and SO_2.

It is known that SO_2 molecule is a Lewis acid and therefore binds to the O_{surf} site (anion site) of barium oxide which is a Lewis base. Therefore the adsorption behavior of the SO_2 on barium oxide surface is straightforward. The sulfur atom appears in a position that is above the surface anion (O^{-2}_{surf}) and the O atoms point toward the surface cations (Ba^{+2}_{surf}) (Figure 3.5 (d)).

In the case of NO_2, which can act both as acidic and basic (amphoteric), the adsorption behavior is not simple. For this reason, it is not surprising that there are additional binding configurations for NO_2. Former studies also considered different configurations of NO_2 on BaO surfaces and the corresponding adsorption energies for the same geometries slightly differ due to the implemented calculation methods and size of the cluster or the supercell [28].

3.3.1 NO_2 and SO_2 Adsorptions on Bare BaO (100) Surface

A clean BaO (100) surface which is modeled with a p(2 x 2) slab consisting of four layers with the bottom two layers fixed at the bulk locations while the remaining atoms were allowed to relax.

Various adsorption sites for NO_2 and SO_2 were considered and three distinct relaxed geometries for NO_2, which are presented in Figure 3.5 (a-c), were obtained. When these three adsorption configurations were attempted for SO_2, all of these configurations yield the same geometry which is displayed in Figure 3.5 (d). The results of these calculations are presented in Table 3.6. E_{ads}, d_{ad-S}, α, r_{N-O} and $\Delta\rho$ represent the adsorption energy, the distance between the adsorbate and surface, the bond angle of the adsorbate, the bond length of the adsorbate and the charge transfer from the surface to the adsorbate, respectively.

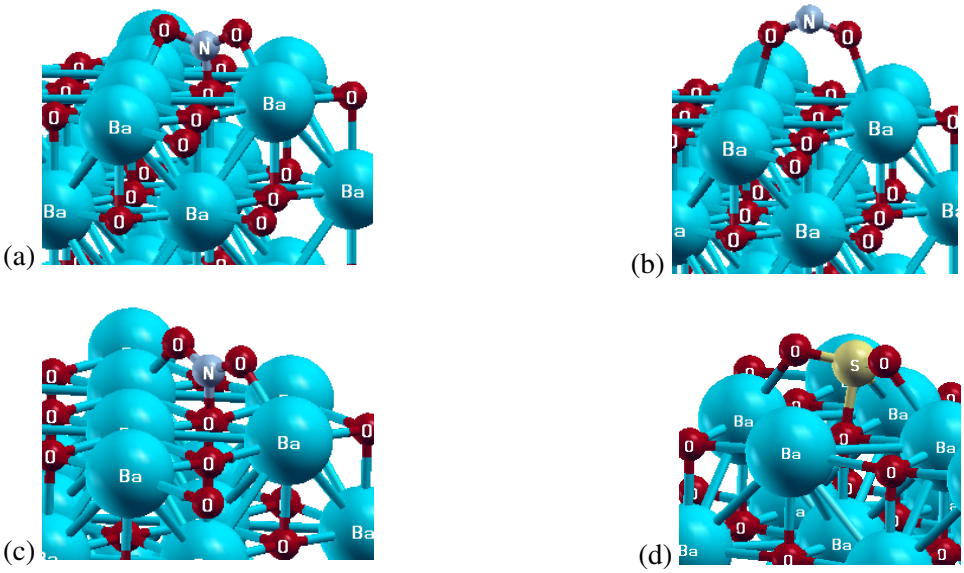

Figure 3.5: Optimized adsorption configurations of NO_2 on bare BaO (100) surface: (a) N-down I, (b) Bridge, and (c) N-down II geometries. Optimized adsorption configuration of SO_2 on BaO (100) surface: (d) S-down.

Table 3.6: Adsorption energies and geometric parameters of NO_2 and SO_2 on bare BaO (100) surface. The results of previous works [45, 50, 54] are in parenthesis.

Conf.	E_{ads} [eV]	d_{ad-S} [Å]	α [°]	r_{N-O} [Å]	$\Delta\rho$ [$\|e\|$]
N-down I	-1.43 (-1.52 [45])	1.45 (1.44)	120 (121)	1.32 (1.32)	0.88 (0.90 [50])
Bridge	-1.66 (-1.43 [45])	2.77 (2.75)	116 (116)	1.27 (1.28)	0.81 (0.80 [50])
N-down II	-1.30 (-1.30 [54])	1.48 (1.44)	117 (121)	1.31 (1.31)	0.85
S-down	-2.72 (-2.60 [45])	1.64 (1.64)	108 (104)	1.53 (1.52)	0.54 (0.53 [50])

As it can be seen from the table, the results of our calculations agree with the results of the former studies. Therefore, this information proves that the results are accurate and does not strongly depend on the choice of the models used.

The adsorption energy of SO_2 is much higher than all of the NO_2 configurations due to the stronger Lewis acidity of the SO_2. The energy values indicate strong surface adsorption which are backed up by the lengthened S–O bond distance (from 1.46 to 1.53) and narrowed O–S–O bond angle (from 119 to 108) due to the strong interaction with the substrate.

The adsorption of the NO_2 molecule is ruled by several factors in which the charge transfer is the most effective one. The basicity of the surface governs the charge transfer from the adsorbent to the adsorbate. Depending on the charge transfer, which is also related to acting as electron donor or acceptor, several binding sites are available for the adsorbate. The charge

transfer values were acquired by Löwdin population analysis [57] which suggests that all NO_2 adsorptions are acidic on bare BaO (100) surface. For all of the binding modes, the N–O bond length elongated and the O–N–O angle decreased. Only the bridge configuration was adsorbed as a nitrite with a near-complete transfer of one electron from surface to NO_2 whereas N-down I and II binding modes were adsorbed as nitrate (d(N–O)=1.25 Å , α(O–N–O)=120° [53]). The difference between N-down I and II adsorption configurations is that the former bridges two neighboring Ba_{surf} atoms whereas the latter bridges two diagonal Ba_{surf} atoms. Since barium oxide is quite a strong base, NO_2 molecule binded to the substrate more strongly with high perturbation of the adsorbate geometry as it can be seen from the adsorption energies and geometric parameters reported in Table 3.6.

3.3.2 NO_2 and SO_2 Adsorptions on the doped BaO (100) Surfaces

Various adsorption configurations of NO_2 and SO_2 were tested on the doped barium oxide (100) surface. The stability of these configurations vary depending on the introduced dopant. For example, some of the adsorption geometries were not observed for some doped surfaces while additional stable geometries were found in some cases. The stability of the adsorption configurations can be related to different covalent radius and oxidation state of the dopants introduced [58].

In order to test the impact of the dopants on the BaO (100) surface, a surface Ba atom (Ba_{surf}) of a clean barium oxide surface was replaced by a dopant and the four layered slab was further relaxed. All of the dopants were replacing the same Ba_{surf} atom. After the geometry optimization step, NO_2 or SO_2 was added and further geometry optimization was carried out.

3.3.2.1 NO_2 and SO_2 Adsorptions on K-Doped BaO (100) Surface

The effect of the different oxidation state is investigated by introducing the K atom to the BaO surface. The covalent radius of K (1.96 Å [59]) is close to the covalent radius of the barium (1.98 Å [58]) and the oxidation state of K is +1 whereas it is +2 for Ba. This difference on the oxidation states were proven by the Löwdin population analysis as well. The adsorption modes of NO_2 and SO_2 over K-doped BaO (100) surface are presented in Figure 3.6 and the geometric parameters of these configurations are reported in Table 3.7.

Figure 3.6: Optimized adsorption geometries of NO_2 on K-doped BaO (100) surface: (a) Bridge, (b) Tilted, (c) N-down II. Optimized adsorption geometry of SO_2 on K-doped BaO (100) surface: (d) S-down.

Table 3.7: Adsorption energies and geometric parameters of NO_2 and SO_2 on K-doped BaO (100) surface. The results of bare BaO (100) surface are in parenthesis.

Conf.	E_{ads} [eV]	d_{ad-S} [Å]	α [°]	r_{N-O} [Å]	$\Delta\rho$ [$\|e\|$]
Bridge	-1.38 (-1.66)	2.70 (2.77)	117 (116)	1.27 (1.27)	0.73 (0.81)
Tilted	-2.32	1.32	123	1.26	0.28
N-down II	-2.41 (-1.30)	1.32 (1.48)	123 (117)	1.25 (1.31)	0.29 (0.85)
S-down	-2.72 (-2.72)	1.64 (1.64)	108 (108)	1.53 (1.53)	0.53 (0.54)

In the case of the K-doped BaO (100) surface, there was an additional NO_2 adsorption site with a high binding energy and this geometry is not reported in any of the previous works. The geometric parameters of adsorbed NO_2 on this binding mode indicate that the tilted configuration was adsorbed as a nitrate exceeding the ideal bond length by 0.01 Å and the bond angle by 3°. For the bridge configuration the binding energy decreased surprisingly as the charge transfer did not considerably change. The binding energy of the nitrate-like N-down II configuration increased appreciably with a very low charge transfer. It can be concluded that due to the different oxidation state of K, this surface favors the nitrate-like adsorption with low charge transfer. Even though K-doped BaO (100) surface does not increase the sulfur tolerance as reported by Toops et al. [58], it favors NO_2 adsorption.

In order to test the effect of the coverage, a second Ba_{surf} atom from the K-doped BaO (100)

surface was replaced by another K atom and this four layered slab was also relaxed.After the geometry optimization step, NO_2 or SO_2 was added to this slab and the surface studies were performed. The resulting binding modes of adsorbates over 2K-doped BaO (100) surface is displayed in Figure 3.7 and the results of the calculations are presented in Table 3.8.

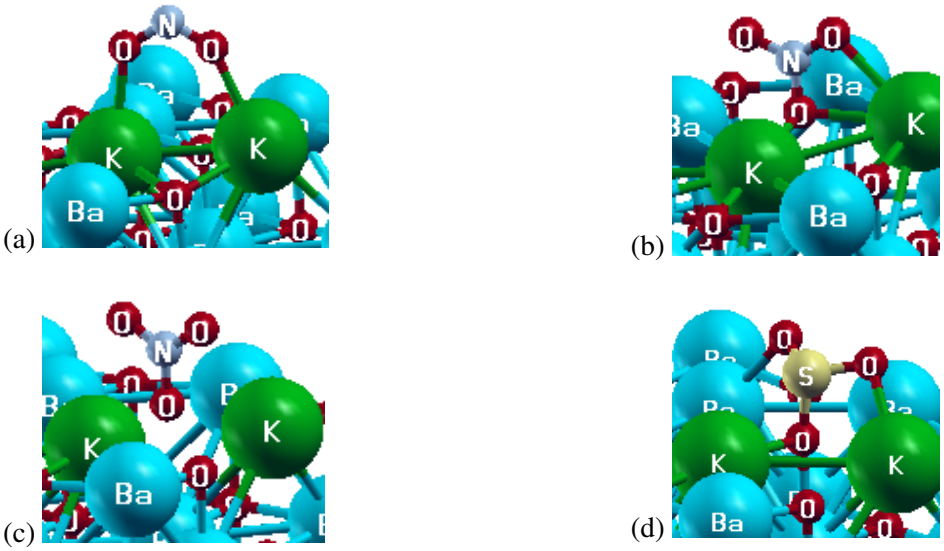

Figure 3.7: Optimized adsorption geometries of NO_2 on 2K-doped BaO (100) surface: (a) Bridge, (b) Tilted, (c) N-down II. Optimized adsorption geometry of SO_2 on 2K-doped BaO (100) surface: (d) S-down.

Table 3.8: Adsorption energies and geometric parameters of NO_2 and SO_2 on 2K-doped BaO (100) surface. The results of K-doped BaO (100) surface are in parenthesis.

Conf.	E_{ads} [eV]	d_{ad-S} [Å]	α [°]	r_{N-O} [Å]	$\Delta\rho$ [$\|e\|$]
Bridge	-1.15 (-1.38)	2.76 (2.70)	119 (117)	1.26 (1.27)	0.62 (0.73)
Tilted	-2.71 (-2.32)	1.42 (1.32)	108 (123)	1.22 (1.26)	0.29 (0.28)
N-down II	-2.70 (-2.41)	1.32 (1.32)	123 (123)	1.25 (1.26)	0.29 (0.29)
S-down	-2.79 (-2.72)	1.63 (1.64)	107 (108)	1.53 (1.53)	0.53 (0.53)

In the case of the 2K-doped BaO (100) surface all of the binding modes, which were investigated for the single dopant included surface, were tested and the same relaxed geometries with small differences were obtained. The introduction of the second dopant scarcely changed the charge transfer from substrate to the adsorbate. Even though the binding energy of the bridge configuration decreased some more, the introduction of the second K strengthened the NO_2 binding in both the tilted and N-down II configurations. This fact even further proves that

a decreased oxidation state of a surface atom on BaO (100) surface favors the nitrate-like adsorption. In spite of the unimproved sulfur tolerance, it can be deduced that the increased coverage of K on the BaO (100) surface advances the NO_2 adsorption and therefore enhances the NSR catalyst.

3.3.2.2 NO_2 and SO_2 Adsorptions on Ca-Doped BaO (100) Surface

By introducing the Ca atom to the BaO surface, the impact of local lattice strain is investigated. The covalent radius of Ca (1.71 Å [59]) is smaller than Ba (14%). A variety of binding sites of NO_2 exists and these adsorption geometries were tested. Only two adsorption configurations of NO_2 and one adsorption configuration for SO_2 were obtained. The binding modes are displayed in Figure 3.8 and the results of the calculations are reported in Table 3.9.

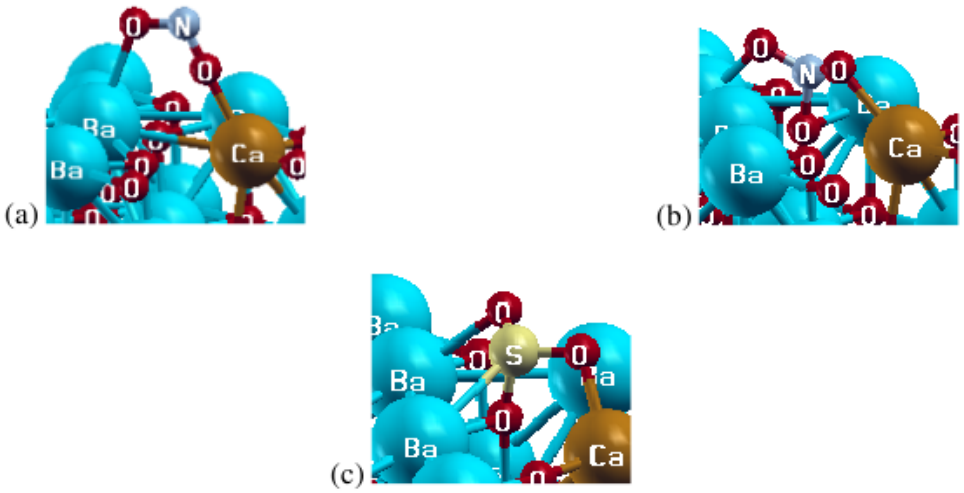

Figure 3.8: Optimized adsorption geometries of NO_2 on Ca-doped BaO (100) surface: (a) Bridge, (b) N-down II. Optimized adsorption geometry of SO_2 on Ca-doped BaO (100) surface: (c) S-down.

Table 3.9: Adsorption energies and geometric parameters of NO_2 and SO_2 on Ca-doped BaO (100) surface. The results of bare BaO (100) surface are in parenthesis.

Conf.	E_{ads} [eV]	d_{ad-S} [Å]	α [°]	r_{N-O} [Å]	$\Delta\rho$ [$\|e\|$]
Bridge	-1.69 (-1.66)	2.37 (2.77)	115 (116)	1.28 (1.27)	0.73 (0.81)
N-down II	-1.56 (-1.30)	1.44 (1.48)	118 (117)	1.32 (1.31)	0.79 (0.85)
S-down	-2.94 (-2.72)	1.62 (1.64)	109 (108)	1.53 (1.53)	0.45 (0.54)

For the Ca introduced BaO (100) surface the adsorption energies for both the bridge and the N-down II configurations increase, especially the N-down II mode which is characterized by smaller adsorbate-substrate distance. Unfortunately, the S-down configuration is also more favored by the Ca-doped barium oxide surface. It can be concluded that local lattice strain influences the NO_2 and SO_2 adsorption by enhancing the interaction with the adsorbates.

The effect of the coverage was also tested for the calcium doped BaO (100) surface when a second Ca atom introduced to the slab. After the geometry optimization step, NO_2 or SO_2 was added to the slab and the surface studies were completed. The binding modes of adsorbates over 2Ca-doped BaO (100) surface is shown in Figure 3.9. Additionally the adsorption energies and geometric parameters of these calculations are reported in Table 3.10.

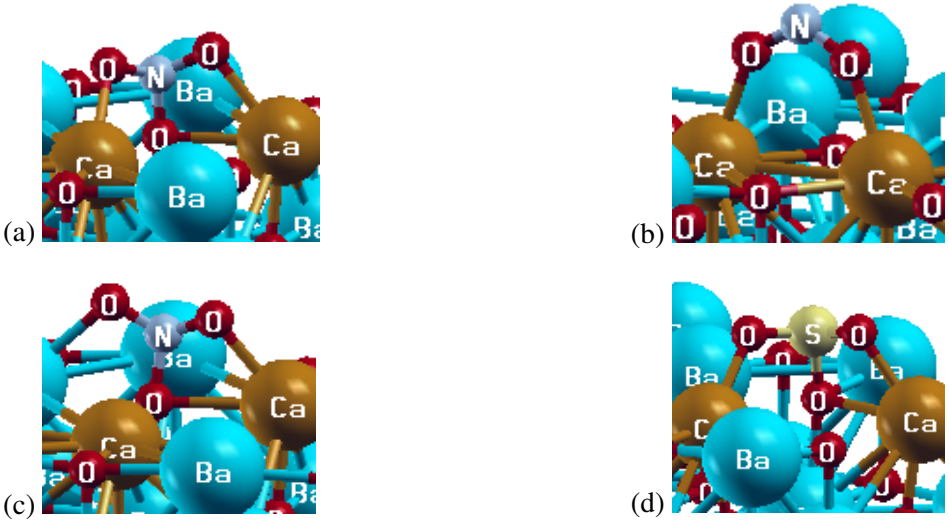

Figure 3.9: Optimized adsorption geometries of NO_2 on 2Ca-doped BaO (100) surface: (a) N-down I, (b) Bridge, (c) N-down II. Optimized adsorption geometries of SO_2 on 2Ca-doped BaO (100) surface: (d) S-down.

Table 3.10: Adsorption energies and geometric parameters of NO_2 and SO_2 on 2Ca-doped BaO (100) surface. The results of Ca-doped BaO (100) surface are in parenthesis. Only the results of the N-down I configuration in parenthesis belongs to bare BaO (100) surface.

Conf.	E_{ads} [eV]	d_{ad-S} [Å]	α [°]	r_{N-O} [Å]	$\Delta\rho$ [$\|e\|$]
N-down I	-1.26 (-1.43)	1.43 (1.45)	121 (120)	1.31 (1.32)	0.70 (0.88)
Bridge	-1.39 (-1.69)	2.46 (2.37)	118 (115)	1.27 (1.28)	0.57 (0.73)
N-down II	-1.21 (-1.56)	1.45 (1.44)	121 (118)	1.31 (1.32)	0.73 (0.79)
S-down	-2.72 (-2.94)	1.62 (1.62)	110 (109)	1.53 (1.53)	0.33 (0.45)

In the case of 2Ca-doped BaO (100) surface, the N-down I adsorption configuration which was only attained by the bare BaO (100) surface was observed unfortunately, with a smaller binding energy and charge transfer. Moreover, despite the unperturbed adsorption geometries, the bridge and N-down II configurations yielded weakened NO_2 binding with smaller charge transfer as in the case of the S-down configuration. The binding energy of the S-down configuration on 2Ca-doped BaO (100) surface decreased back to exactly the same value of the binding energy of the S-down configuration on bare BaO (100) surface. Since SO_2 is a relatively strong Lewis acid, smaller charge transfer is the main reason of this decrease on the binding energy of sulfur dioxide. The introduction of the second Ca on the Ca-doped BaO (100) surface has further increased local lattice strain. However, the increased coverage did not promote the NO_2 adsorption and lowered the binding energy value of the S-down configuration only to that on bare barium oxide surface. Therefore, an increased sulfur tolerance and enhanced NO_2 adsorption could not be achieved by 2Ca-doped BaO (100) surface.

3.3.2.3 NO_2 and SO_2 Adsorptions on La-Doped BaO (100) Surface

The introduction of the lanthanum is done to investigate the effects of different oxidation state since its oxidation state is +3. However, the covalent radius of La (1.69 [58]) is significantly smaller than Ba and therefore it introduces local lattice strain as well. As in the case of the Ca-doped BaO surface, all possible geometries were tested; however similarly, only two binding modes of NO_2 and one binding mode of SO_2 were observed. These adsorption configurations are shown in Figure 3.10 and Table 3.11 summarizes the results of the calculations.

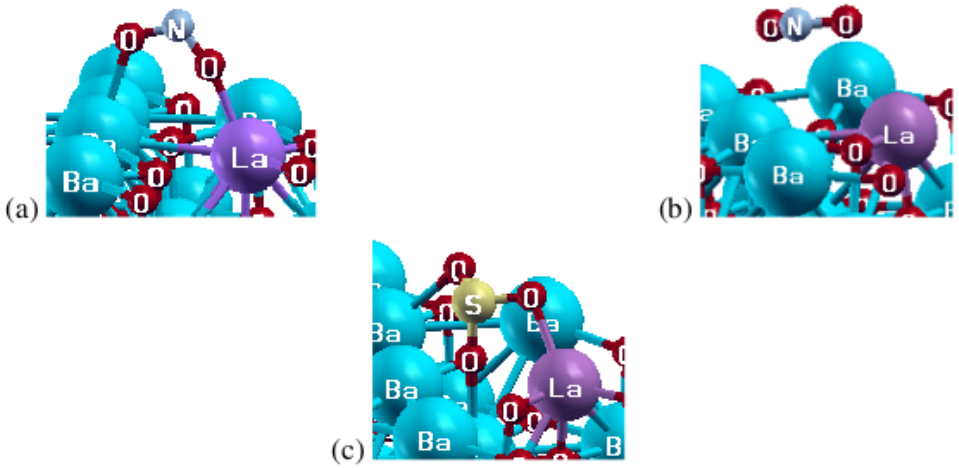

Figure 3.10: Optimized adsorption geometries of NO_2 on La-doped BaO (100) surface: (a) Bridge, (b) Flat. Optimized adsorption geometry of SO_2 on La-doped BaO (100) surface: (c) S-down.

Table 3.11: Adsorption energies and geometric parameters of NO_2 and SO_2 on La-doped BaO (100) surface. The results of our bare BaO (100) surface and a previous work [50] for the flat geometry are in parenthesis.

Conf.	E_{ads} $[eV]$	d_{ad-S} [Å]	α [°]	r_{N-O} [Å]	$\Delta\rho$ $[\|e\|]$
Bridge	-3.54 (-1.66)	2.56 (2.77)	115 (116)	1.27 (1.27)	0.67 (0.81)
Flat	-3.57 (-1.49 [50])	2.88 (2.72)	115 (117)	1.27 (1.27)	0.75 (0.85)
S-down	-2.57 (-2.72)	1.63 (1.64)	108 (108)	1.53 (1.53)	0.35 (0.54)

A rather interesting adsorption profile emerges in the case of the La-doped BaO (100) surface where both N-down I and II configurations are less stable. Instead of these binding modes, with a very high binding energy there is an additional NO_2 adsorption mode (flat) which was also reported in previous works [45, 50]. However, reported adsorption energy of this binding configuration over bare BaO is much lower than the corresponding configuration on La-doped BaO (100) surface. Moreover, the binding energy for the bridge configuration on La-doped BaO surface is also intensely higher than the binding energy of the bridge configuration found for other dopants and in spite of its relatively low charge transfer it is the second largest binding energy for NO_2 adsorption after the flat configuration. In addition, the adsorption energy of the S-down binding mode is reduced to -2.57 eV with a very low charge transfer. In light of these results, it can be concluded that the combination of local lattice strain and an increased oxidation state benefit both the NO_2 adsorption performance and sulfur tolerance.

To test the impact of the coverage, 2La-doped BaO (100) surface was prepared and after the geometry optimization NO_2 or SO_2 was added to the slab. The binding modes of adsorbates over 2La-doped BaO (100) surface is displayed in Figure 3.11 and the results of the calculations are reported in Table 3.12.

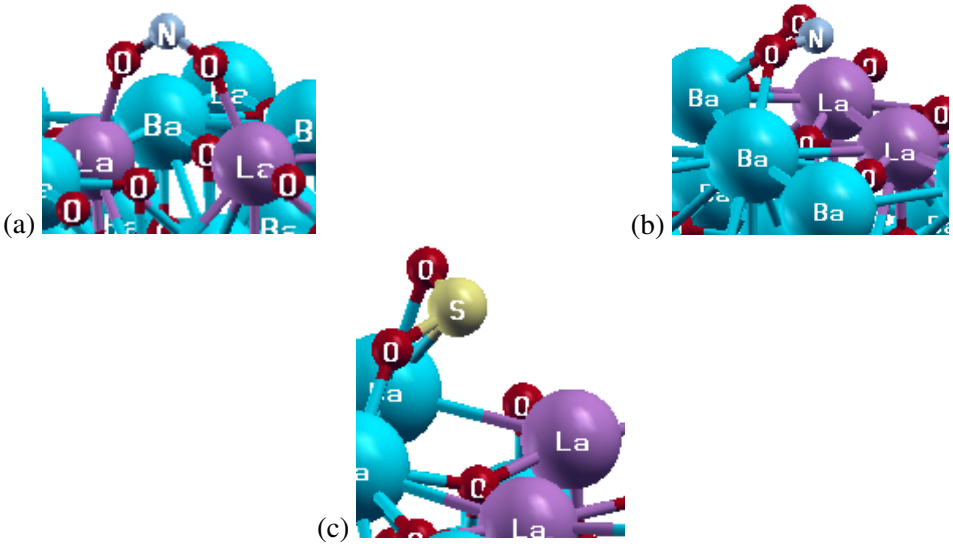

Figure 3.11: Optimized adsorption geometries of NO_2 on 2La-doped BaO (100) surface: (a) Bridge, (b) Flat. Optimized adsorption geometry of SO_2 on 2La-doped BaO (100) surface: (c) S-down.

Table 3.12: Adsorption energies and geometric parameters of NO_2 and SO_2 on 2La-doped BaO (100) surface. The results of La-doped BaO (100) surface are in parenthesis.

Conf.	E_{ads} $[eV]$	d_{ad-S} [Å]	α [°]	r_{N-O} [Å]	$\Delta\rho$ $[\|e\|]$
Bridge	-3.64 (-3.54)	2.53 (2.56)	114 (115)	1.29 (1.27)	0.57 (0.67)
Flat	-3.76 (-3.57)	2.83 (2.88)	112 (115)	1.31 (1.27)	0.95 (0.75)
S-down	-3.03 (-2.57)	2.54 (1.63)	105 (108)	1.60 (1.53)	1.37 (0.35)

For the 2La-doped BaO (100) surface, the binding energies for both the bridge and flat configurations increase. This increase cannot be explained by the insight of the charge transfer and the geometric parameters of the adsorbate. It is due to the replacement of a second Ba atom by another La atom with higher oxidation state. The introduction of the second La strengthened the SO_2 binding in S-down configuration which is characterized by more than a complete charge transfer. In spite of the unimproved sulfur tolerance, it can be deduced that the increased coverage of La on the BaO (100) surface advances the NO_2 adsorption and therefore enhances the storage component of the NSR catalyst.

3.3.2.4 NO_2 and SO_2 Adsorptions on Na-Doped BaO (100) Surface

Finally, in order to investigate both the introduction of local lattice strain and change in the oxidation state, sodium doped BaO surfaces were generated since the covalent radius of Na (1.55 Å [59]) is significantly smaller than Ba and its oxidation state is +1. The adsorption geometries of NO_2 and SO_2 over Na-doped BaO (100) surface are displayed in Figure 3.12 and the results of the calculations are presented in Table 3.13.

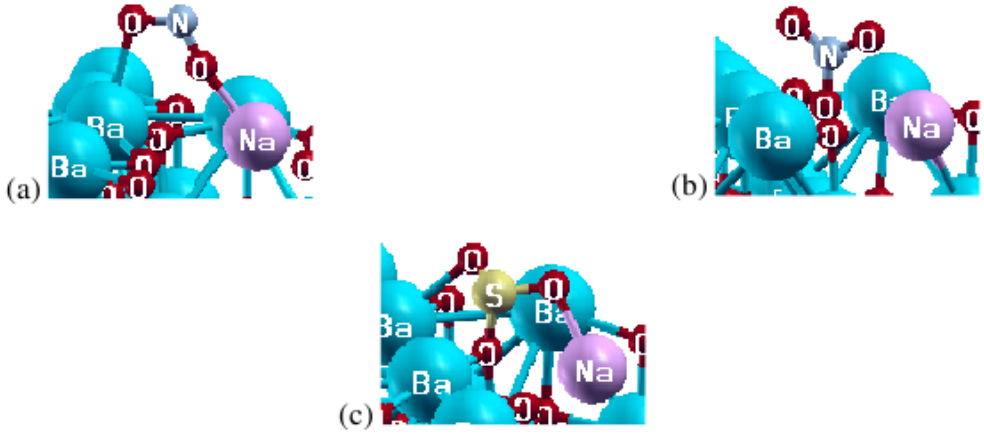

Figure 3.12: Optimized adsorption geometries of NO_2 on Na-doped BaO (100) surface: (a) Bridge, (b) N-down II. Optimized adsorption geometry of SO_2 on Na-doped BaO (100) surface: (c) S-down.

Table 3.13: Adsorption energies and geometric parameters of NO_2 and SO_2 on Na-doped BaO (100) surface. The results of bare BaO (100) surface are in parenthesis.

Conf.	E_{ads} [eV]	d_{ad-S} [Å]	α [°]	r_{N-O} [Å]	$\Delta\rho$ [$\|e\|$]
Bridge	-1.38 (-1.66)	2.33 (2.77)	115 (116)	1.28 (1.27)	0.81 (0.81)
N-down II	-2.39 (-1.30)	1.32 (1.48)	123 (117)	1.25 (1.31)	0.29 (0.85)
S-down	-2.78 (-2.72)	1.62 (1.64)	108 (108)	1.52 (1.53)	0.53 (0.54)

For the Na-doped BaO (100) surface the N-down II configuration is more stable with an increase of 1 eV on the adsorption energy in spite of very low charge transfer as in the case of the N-down II configuration over K-doped BaO (100) surface. The geometric parameters of the adsorbate indicate a nitrate-like adsorption with only a small perturbation on the bond angle (3°). However, the adsorption energy of the bridge configuration is reduced to -1.38 eV

with a decrease of 0.28 eV. This can be due to the small covalent radius of Na which causes a reduction on the distance between oxygen atom of NO_2 and Na_{surf} and therefore results in a deviation from the nitrite-like adsorption mode. Unfortunately, the S-down configuration is slightly more favored by the Na-doped barium oxide surface. It can be concluded that the combination of local lattice strain and different oxidation state of the dopant on BaO (100) surface does not yield a major impact on the sulfur poisoning. However, for this dopant NO_2 adsorption is found to be competing with SO_2 adsorption. For this reason, the Na-doped BaO (100) surface can be a viable storage material for the NSR catalysts.

The effect of the coverage was also tested for the Na-doped BaO (100) surface by doping a second Na atom to the slab. The binding modes of NO_2 and SO_2 over 2Na-doped BaO (100) surface and their geometric parameters are shown in Figure 3.13 and Table 3.14, respectively.

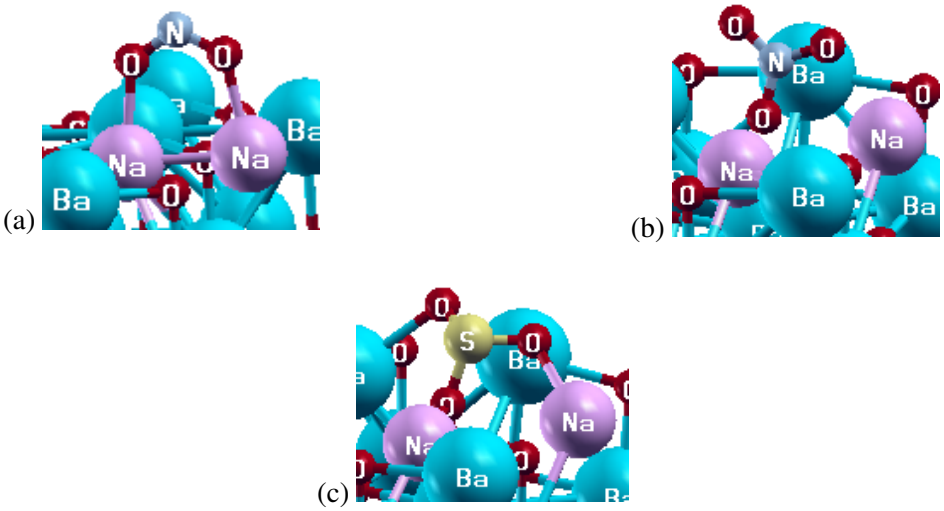

Figure 3.13: Optimized adsorption geometries of NO_2 on 2Na-doped BaO (100) surface: (a) Bridge, (b) N-down II. Optimized adsorption geometry of SO_2 on 2Na-doped BaO (100) surface: (c) S-down.

Table 3.14: Adsorption energies and geometric parameters of NO_2 and SO_2 on 2Na-doped BaO (100) surface. The results of Na-doped BaO (100) surface are in parenthesis.

Conf.	E_{ads} $[eV]$	d_{ad-S} [Å]	α [°]	r_{N-O} [Å]	$\Delta\rho$ $[\|e\|]$
Bridge	-1.11 (-1.38)	2.38 (2.33)	119 (115)	1.26 (1.28)	0.63 (0.81)
N-down II	-2.84 (-2.39)	1.31 (1.32)	122 (123)	1.25 (1.25)	0.29 (0.29)
S-down	-2.99 (-2.78)	1.61 (1.62)	106 (108)	1.54 (1.52)	0.55 (0.53)

In the case of the 2Na-doped BaO (100) surface, the adsorption energy of the bridge configuration is further reduced to -1.11 eV with a decrease of 0.55 eV with respect to the bare BaO (100) surface. On the contrary, the introduction of the second Na strengthened NO_2 binding in N-down II configuration as in the case of the 2K-doped BaO (100) surface. SO_2 adsorption is even more enhanced than Na introduced BaO (100) surface. In spite of the unimproved sulfur durability, it can be deduced that the increased coverage of Na on the BaO (100) surface promotes NO_2 adsorption and yields competitive NO_2 binding.

3.3.3 NO_2 and SO_2 Adsorptions on Alkali Metal Oxide Surfaces

3.3.3.1 Alkali Metal Oxide (100) Surface

Only a small set of adsorption geometries on a p(1 x 1) slab consisting of five layers with the bottom two layers fixed was tested on these surfaces with the aim to understand whether these storage materials have a promising potential for the abatement of NO_x from the exhaust of the lean-burn engines. The adsorption configurations of NO_2 and SO_2 over Li_2O (100) surface are presented in Figures 3.14 and the result of these calculations are given in Table 3.15.

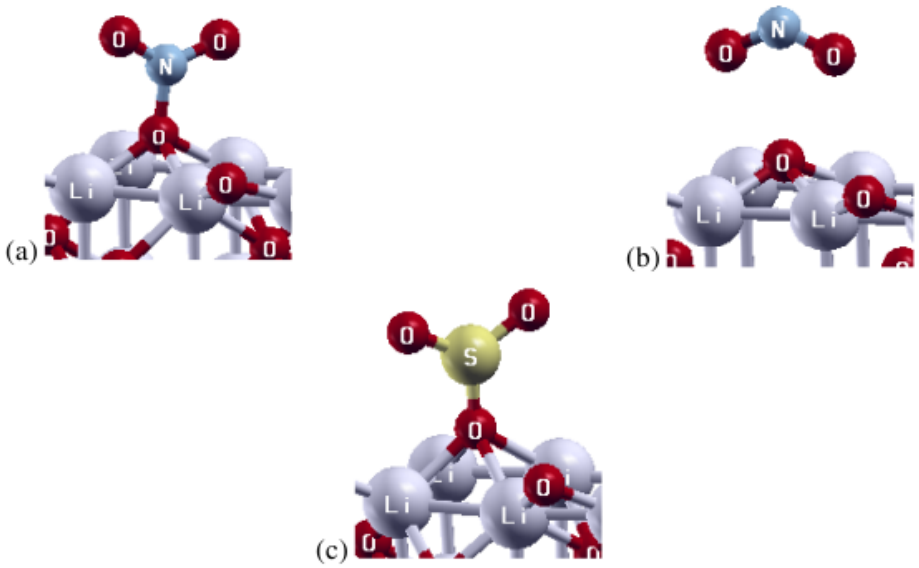

Figure 3.14: Optimized adsorption geometries of NO_2 on Li_2O (100) surface: (a) N-down II, (b) O-down. Optimized adsorption geometry of SO_2 on Li_2O (100) surface: (c) S-down.

It can be seen from Table 3.15 that N-down II configuration yields a very high adsorption

Table 3.15: Adsorption energies and geometric parameters of NO_2 and SO_2 on (100) surface of Li_2O.

Conf.	E_{ads} [eV]	d_{ad-S} [Å]	α [°]	r_{N-O} [Å]	$\Delta\rho$ [$\|e\|$]
N-down II (NO_2)	-2.75	1.42	128	1.22	0.25
O-down (NO_2)	-0.81	2.10	130	1.19	0.36
S-down (SO_2)	-1.91	1.49	120	1.42	0.95

energy with a very low charge transfer which implies that even though the charge transfer from surface to the adsorbate is small, NO_2 molecule can be more stable. The S-down configuration has the lowest adsorption energy among all of the tested slabs. The O-down binding mode has a very low adsorption energy of -0.81 eV and the structure of the adsorbate approaches the structure of the gas phase NO_2 molecule indicating physisorption. We conclude that the enhanced chemisorption of NO_2 and the increased sulfur tolerance observed for the Li_2O (100) surface could suggest a possible practical application as storage material in NSR catalysts, barring issues related to its stability under working conditions of the catalysts.

The adsorption configurations of NO_2 and SO_2 over Na_2O (100) surface are presented in Figures 3.15 and the result of these calculations are given in the Table 3.16.

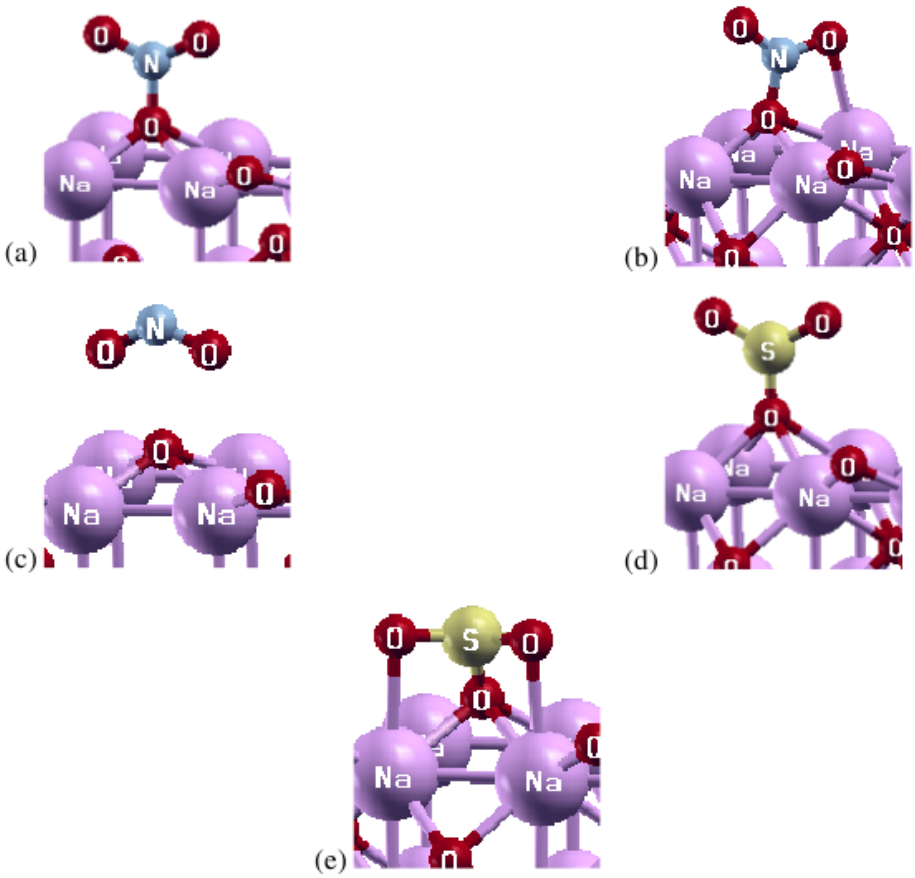

Figure 3.15: Optimized adsorption geometries of NO_2 on Na_2O (100) surface: (a) N-down II, (b) Tilted, (c) O-down. Optimized adsorption geometries of SO_2 on Na_2O (100) surface: (d) S-down, (e) Bidentate.

Table 3.16: Adsorption energies and geometric parameters of NO_2 and SO_2 on (100) surface of Na_2O.

Slab	E_{ads} [eV]	d_{ad-S} [Å]	α [°]	r_{N-O} [Å]	$\Delta\rho$ [$\|e\|$]
N-down II (NO_2)	-3.26	1.40	128	1.23	0.02
Tilted (NO_2)	-3.31	1.39	128	1.24	0.02
O-down (NO_2)	-0.96	2.06	128	1.20	0.17
S-down (SO_2)	-2.27	1.49	125	1.44	0.79
Bidentate (SO_2)	-2.57	1.56	122	1.48	0.36

For the case of the Na_2O (100) surface, we observe a strong NO_2 chemisorption over the adsorbent and the binding energies of both SO_2 adsorption configurations are low. As in the case of the corresponding O-down geometry on Li_2O (100) surface, NO_2 molecule physisorbs with a very low binding energy. The structural parameters of NO_2 for both the N-down II and tilted binding modes consistent with a nitrate-like adsorption description with non-existent

charge transfer. The binding energies of these configurations are higher than the binding energies of both of the SO_2 configurations. It can be concluded that the Na_2O (100) surface favors NO_2 adsorption over SO_2 adsorption and it could be a suitable storage material for the NO_x storage and reduction catalysts.

The adsorption configurations of NO_2 and SO_2 over K_2O (100) surface are presented in Figures 3.16 and the result of these calculations are given in Table 3.17.

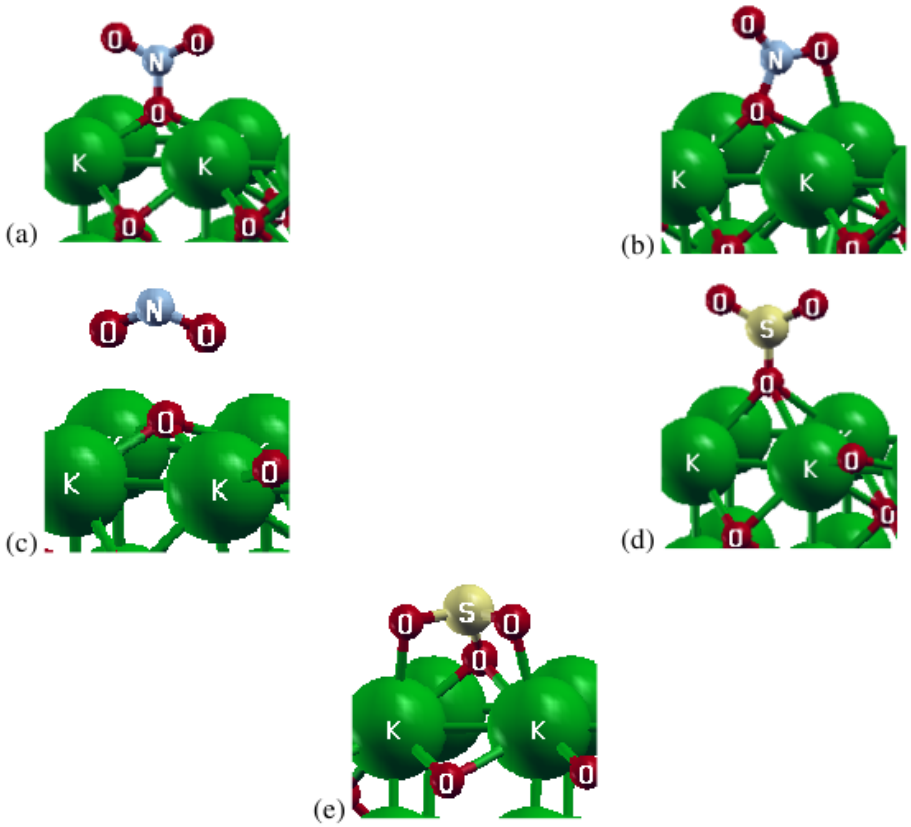

Figure 3.16: Optimized adsorption geometries of NO_2 on K_2O (100) surface: (a) N-down II, (b) Tilted, (c) O-down. Optimized adsorption geometries of SO_2 on K_2O (100) surface: (d) S-down, (e) Bidentate.

Table 3.17: Adsorption energies and geometric parameters of NO_2 and SO_2 on (100) surface of K_2O.

Conf.	E_{ads} [eV]	d_{ad-S} [Å]	α [°]	r_{N-O} [Å]	$\Delta\rho$ [$\|e\|$]
N-down II (NO_2)	-3.84	1.34	125	1.25	0.20
Tilted (NO_2)	-3.92	1.34	124	1.27	0.21
O-down (NO_2)	-0.69	2.03	126	1.21	0.03
S-down (SO_2)	-1.90	1.49	124	1.45	0.68
Bidentate (SO_2)	-3.53	1.60	108	1.53	0.32

It can be seen from Table 3.13 that NO_2 adsorption on K_2O (100) surface follows the same trend as that on the Na_2O (100) surface. There is strong NO_2 chemisorption over the adsorbent and the binding energy of the S-down geometry is very low. As in the case of the O-down geometry on Li_2O and Na_2O surfaces, NO_2 molecule physisorbs in the O-down configuration on K_2O surface with a very low binding energy and charge transfer. In spite of the resemblance of the geometric parameters of the bidentate configuration on K_2O and Na_2O surfaces, there is a sharp increase on the binding energy of this geometry on K_2O surface. This might be due to the relatively higher basicity of the K_2O surface compared to the Na_2O surface. To conclude, it can be said that since both of the binding modes of the chemisorbed NO_2 are characterized by very high binding energies which are even larger than the binding energies of both of the SO_2 configurations, the K_2O is an adequate storage material for the NSR catalysts.

It should be noted once again that a small set of adsorption geometries on a p(1 x 1) slab consisting of five layers was tested on the (100) surface of these alkali metals. These slabs are small cells, so further studies will include larger cells, say p(2 x 2) slabs.

3.3.3.2 Alkali Metal Oxide (110) Surface

The results of these preliminary test calculations suggest that alkali metal oxides are promising storage materials for NSR catalysts. We also considered the stoichiometric surface (110) of alkali metal oxides. Various binding modes of NO_2 and SO_2 on a p(2 x 1) slab consisting of five layers were tested on the (110) surface. In the case of the (110) surface of Li_2O, all of the NO_2 and SO_2 configurations did not give any interesting result and are therefore not included. The optimized geometries for adsorption over Na_2O are displayed in Figure 3.17 and Table 3.18.

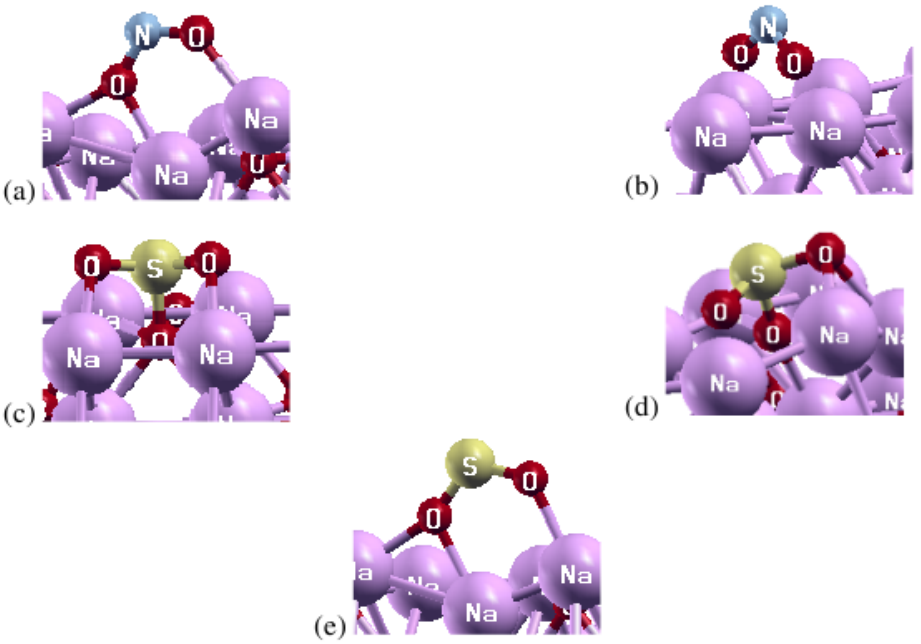

Figure 3.17: Optimized adsorption geometries of NO_2 on Na_2O (110) surface: (a) N-up and (b) O-down. Optimized adsorption geometries of SO_2 on Na_2O (110) surface: (c) Bidentate, (d) Tilted and (e) S-up.

Table 3.18: Adsorption energies and geometric parameters of NO_2 and SO_2 over (110) surface of Na_2O.

Conf.	E_{ads} [eV]	d_{ad-S} [Å]	α [°]	r_{N-O} [Å]	$\Delta\rho$ [$\|e\|$]
N-up (NO_2)	-1.80	2.36	115	1.25	0.77
O-down (NO_2)	-1.66	2.49	114	1.28	0.80
Bidentate (SO_2)	-2.85	1.64	111	1.53	0.47
Tilted (SO_2)	-3.11	1.61	107	1.53	0.49
S-up (SO_2)	-0.89	2.37	114	1.51	0.55

For the case of the Na_2O (110) surface, we observe a strong SO_2 chemisorption over the adsorbent. Additionally, SO_2 molecule physisorbs S-up configuration which is characterized by a very low binding energy . The binding energies of both the NO_2 adsorption configurations and the charge transfers from substrate to the adsorbate are low. Since the Na_2O (110) surface neither promotes NO_2 adsorption nor increases sulfur tolerance, it can be concluded that this surface is not a suitable storage material for the NO_x storage and reduction catalysts.

Two binding configurations of NO_2 and two binding configurations of SO_2 were obtained for the K_2O (110) surface. These adsorption configurations are shown in Figure 3.18 and Table

3.19 summarizes the results of the calculations.

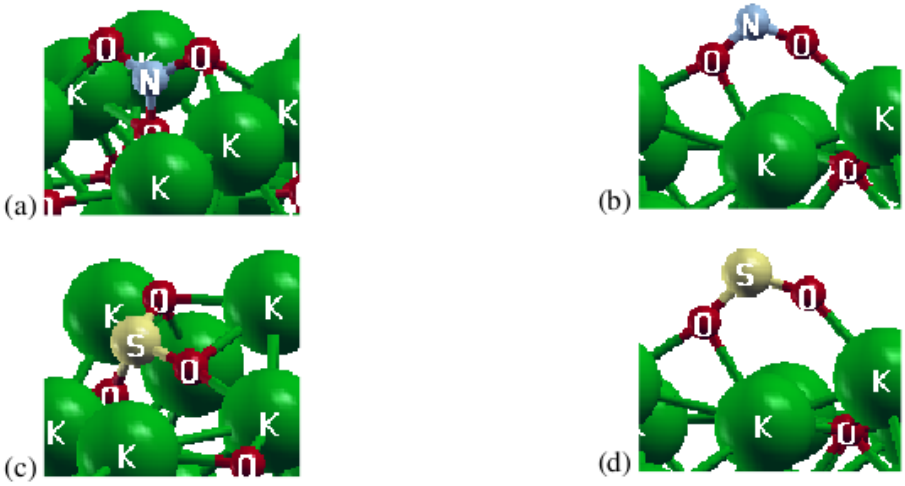

Figure 3.18: Optimized adsorption geometries of NO_2 on K_2O (110) surface: (a) N-down II and (b) N-up. Optimized adsorption geometries of SO_2 on K_2O (110) surface: (c) Bidentate and (d) S-up.

Table 3.19: Adsorption energies and geometric parameters of NO_2 and SO_2 over (110) surfaces of K_2O.

Conf.	E_{ads} [eV]	d_{ad-S} [Å]	α [°]	r_{N-O} [Å]	$\Delta\rho$ [$\|e\|$]
N-down II (NO_2)	-2.14	1.40	120	1.32	0.79
N-up (NO_2)	-2.54	2.65	115	1.29	0.84
Bidentate (SO_2)	-4.21	1.58	107	1.56	0.56
S-up (SO_2)	-1.45	2.65	112	1.54	0.77

Although a very strong SO_2 chemisorption over the K_2O (110) surface is observed, this surface is a suitable storage material for the NO_x storage and reduction catalysts due to the formation of more stable NO_2 adsorption configurations over the surface. In spite of having appreciably high charge transfer value, the S-up binding geometry has a very low adsorption energy.

3.3.4 NO_2 and SO_2 Adsorptions on Alkali Metal over the TiO_2 (001) Surfaces

It is known that TiO_2 has higher sulfur durability as a support material of the NSR catalysts [32] and therefore it is widely studied. However, the NO_x storage capacity of TiO_2 is low.

To investigate the possibility of an increase in the NO_x storage capacity of TiO_2, alkali metal (Li, Na and K) loaded TiO_2 surfaces were generated and various adsorption configurations of NO_2 and SO_2 over these surfaces were tested. For investigating the performance of the alkali metal-loaded TiO_2 (001) surface, primarily the adsorptions of NO_2 and SO_2 in several geometries on bare TiO_2 (001) surface were performed. However, none of the tested binding configurations yielded a sensible adsorption geometry since the NO_2 and SO_2 storage capacity of the TiO_2 is low. As a consequence, the comparison of the adsorption energies between the alkali metal-loaded TiO_2 (001) surface and bare TiO_2 (001) surface cannot be accomplished.

3.3.4.1 NO_2 and SO_2 Adsorptions on Li-loaded TiO_2 (001) Surface

A variety of adsorption configurations of NO_2 and SO_2 over the Li-loaded TiO_2 (001) surface was tested. The resulting binding configurations are displayed in Figure 3.19. Adsorption energies and geometric parameters of adsorbates are summarized in Table 3.20.

Table 3.20: Adsorption energies and geometric parameters of NO_2 and SO_2 on Li-loaded TiO_2 (001) surface.

Conf.	E_{ads} $[eV]$	d_{ad-S} [Å]	α [°]	r_{N-O} [Å]	$\Delta\rho$ $[\|e\|]$
Monodentate (NO_2)	-1.96	1.87	119	1.30	0.36
Bridge (NO_2)	-2.55	1.91	112	1.37	0.51
Bidentate (NO_2)	-2.11	2.04	117	1.27	0.48
Bridge (SO_2)	-1.16	1.93	106	1.57	0.50
Monodentate (SO_2)	-1.32	1.88	115	1.51	0.21
Bidentate (SO_2)	-1.29	2.13	110	1.51	0.21

It can be seen from Table 3.20 that NO_2 adsorption on Li-loaded TiO_2 (001) surface is more stable than SO_2 adsorption for all binding configurations. All NO_2 adsorptions are nitrite-like on this surface and all charge transfers from substrate to adsorbate are low compared to the other surfaces. It can be concluded that the Li-loaded TiO_2 (001) surface favors nitrite-like adsorption. It was already known that TiO_2 has high sulfur durability and low NO_x storage capacity. By adding Li atom to the TiO_2 (001) surface, an appreciably increased NO_x storage capacity was attained and a high sulfur tolerance was sustained. For this reason, the Li-loaded TiO_2 (001) surface is an adequate storage material for the NSR catalysts.

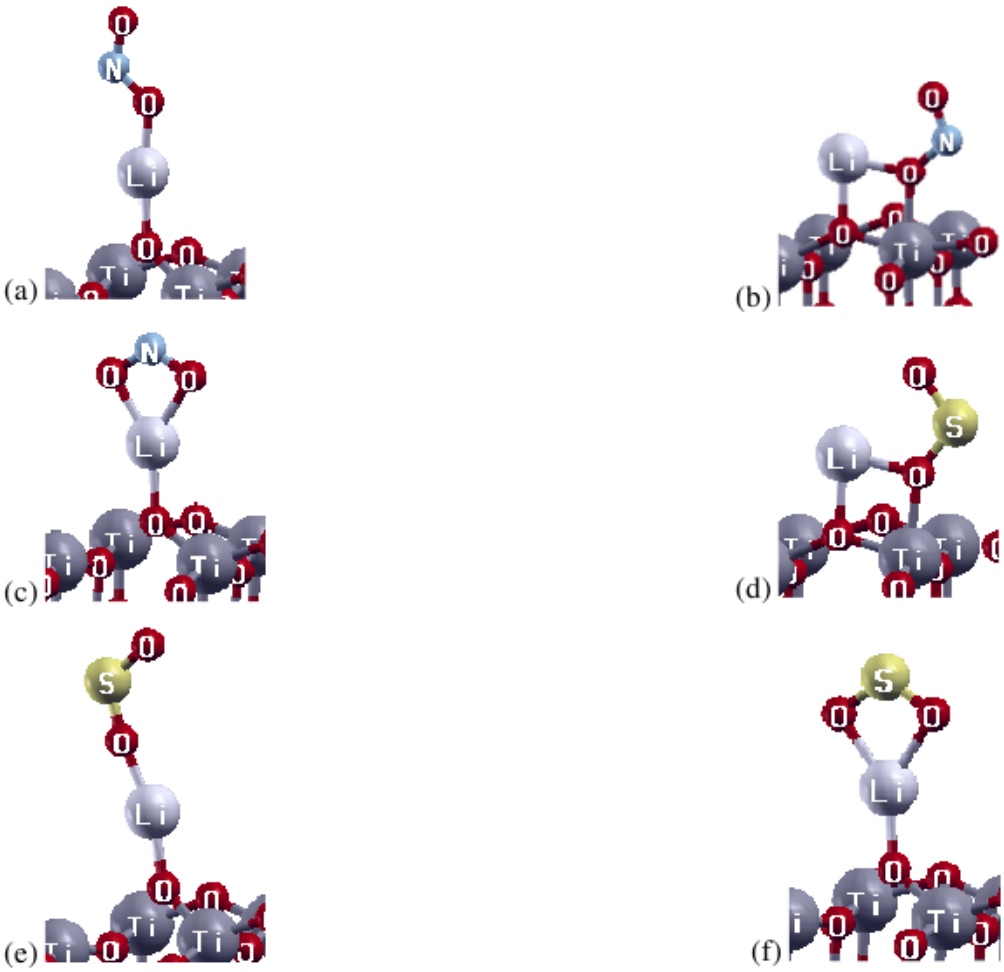

Figure 3.19: Optimized adsorption geometries of NO_2 on Li-loaded TiO_2 (001) surface: (a) Monodentate, (b) Bridge and (c) Bidentate. Optimized adsorption geometries of SO_2 on Li-loaded TiO_2 (001)surface: (d) Bridge, (e) Monodentate and (f) Bidentate.

3.3.4.2 NO_2 and SO_2 Adsorptions on Na-loaded TiO_2 (001) Surface

The binding geometries that were tested on Li-loaded TiO_2 surface were also considered for the Na-loaded TiO_2 surface and the resulting adsorption configurations of NO_2 and SO_2 are presented in Figure 3.20 and the results of the calculations are presented in the Table 3.21.

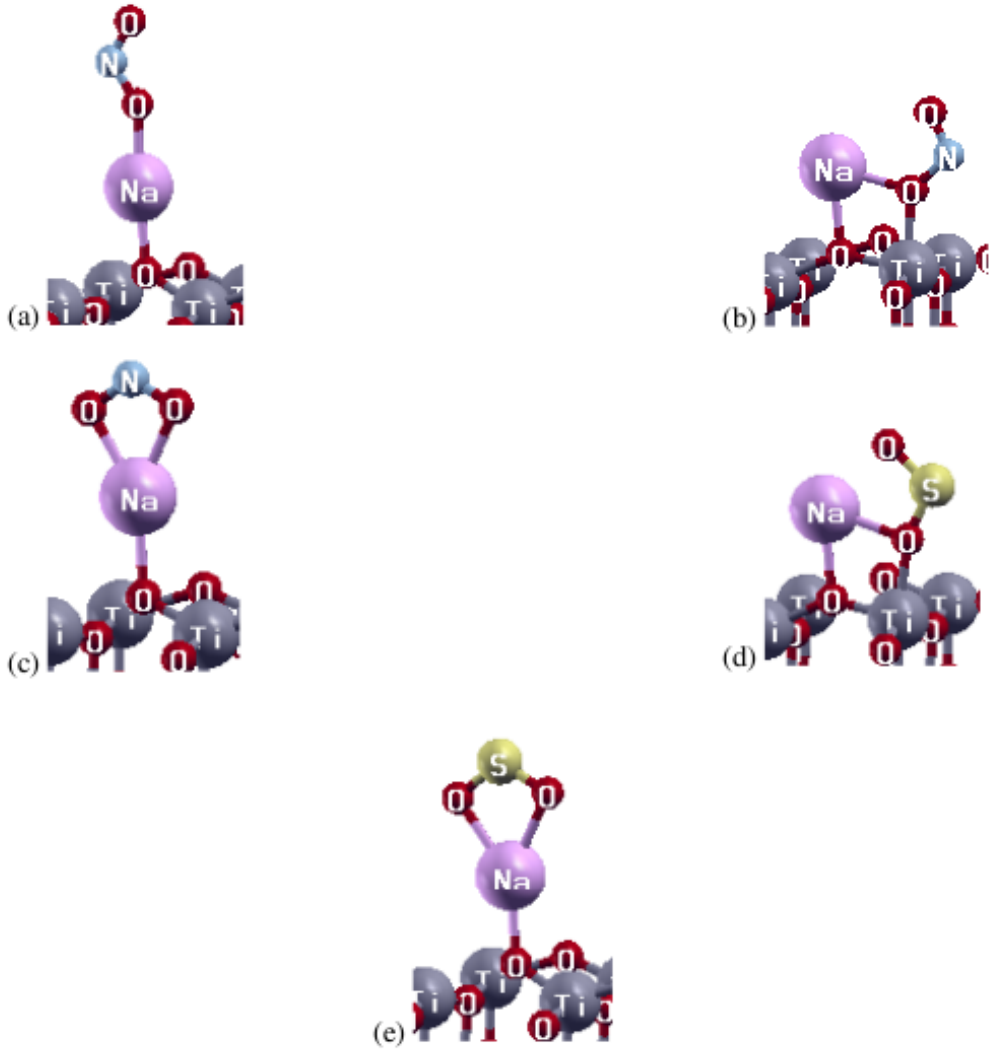

Figure 3.20: Optimized adsorption geometries of NO_2 on Na-loaded TiO_2 (001) surface: (a) Monodentate, (b) Bridge and (c) Bidentate. Optimized adsorption geometries of SO_2 on Na-loaded TiO_2 (001)surface: (d) Bridge and (e) Bidentate.

Table 3.21: Adsorption energies and geometric parameters of NO_2 and SO_2 on Na-loaded TiO_2 (001) surface.

Conf.	E_{ads} [eV]	d_{ad-S} [Å]	α [°]	r_{N-O} [Å]	$\Delta\rho$ [$\|e\|$]
Monodentate (NO_2)	-1.91	2.13	120	1.29	0.52
Bridge (NO_2)	-2.88	2.21	112	1.35	0.67
Bidentate (NO_2)	-2.28	2.30	118	1.26	0.63
Bridge (SO_2)	-1.60	2.32	106	1.55	0.67
Bidentate (SO_2)	-1.47	2.39	111	1.51	0.44

As compared to the NO_2 adsorption on Li-loaded TiO_2 (001) surface, more stable NO_2 ad-

sorption configurations are obtained. Furthermore, the binding energies of the SO_2 adsorption configurations increase as well. All NO_2 adsorptions are nitrite-like as in the case of Li-loaded TiO_2 (001) surface. Addition of Na atom to the TiO_2 (001) surface results in a highly increased NO_x storage capacity and sustained the high sulfur tolerance. For this reason, the Na-loaded TiO_2 (001) surface is a very adequate storage material for the NSR catalysts.

3.3.4.3 NO_2 and SO_2 Adsorptions on K-loaded TiO_2 (001) Surface

Various adsorption geometries of NO_2 and SO_2 on K-loaded TiO_2 (001) surface were also tested as an extension of the results of other alkali metal-loaded TiO_2 surfaces. Only two distinct geometries for NO_2 and two configurations for SO_2 were obtained for this surface. The resulting geometries are displayed in Figure 3.21 and the results of these calculations are reported in Table 3.22.

Figure 3.21: Optimized adsorption geometries of NO_2 on K-loaded TiO_2 (001) surface: (a) Bridge and (b) Bidentate. Optimized adsorption geometries of SO_2 on K-loaded TiO_2 (001) surface: (c) Bridge and (d) Bidentate.

Table 3.22: Adsorption energies and geometric parameters of NO_2 and SO_2 on K-loaded TiO_2 (001) surface.

Conf.	E_{ads} [eV]	d_{ad-S} [Å]	α [°]	r_{N-O} [Å]	$\Delta\rho$ [$\|e\|$]
Bridge (NO_2)	-2.87	2.60	112	1.34	0.69
Bidentate (NO_2)	-1.99	2.65	119	1.26	0.62
Bridge (SO_2)	-1.84	2.69	109	1.52	0.62
Bidentate (SO_2)	-1.26	2.79	113	1.50	0.44

It can be seen from Table 3.22 that NO_2 adsorption on K-loaded TiO_2 (001) surface is more stable than SO_2 adsorption for all binding configurations. However, if we compare the results of the Li- or Na-loaded TiO_2 (001) surface, we will see that the binding energy of the bidentate (NO_2) configuration decreases and the binding energy of the bridge (SO_2) configuration increases. It can be concluded that since all of the adsorption energies of the NO_2 binding configurations are higher than the adsorption energies of the SO_2 binding configurations, K-loaded TiO_2 (001) surface is an adequate storage material for the NSR catalysts. However, it is not as adequate as the Li- or Na-loaded TiO_2 (001) surface.

CHAPTER 4

CONCLUSION

Increasing emission of green-house gases due to high fuel consumption of gasoline engines and industrial applications requires new strategies for preserving clean air. However, these strategies fail to decrease NO_x emission. The emission of these highly noxious pollutants, NO_x, breeds both environmental and health problems. The NO_x storage-reduction (NSR) catalysts have been steadily developed to unravel the issues due to NO_x emission. In this thesis dopants introduced onto BaO (100) surface, alkali metal oxide (100) and (110) surfaces and TiO_2 (001) surface were investigated as a component of NSR.

Preliminary calculations for obtaining the lattice constants and suitable k-point meshes were performed, followed by adsorption studies of NO_2 and SO_2 molecules. The results of these preliminary test calculations were further substantiated by surface energy calculations.

The dopants introduced were chosen with the aim of examining the impacts of the different covalent radius (local lattice strain) and oxidation states with respect to the host materials. Calculated binding energies of NO_2 and SO_2 species on doped BaO (100) surface revealed that the presence of the dopant increases the stability of NO_2 adsorption in most cases. The La doped BaO (100) surface has the most stable NO_2 adsorption among the other dopants included BaO (100) surfaces. This result suggests that the combination of local lattice strain and an increased oxidation state benefit both NO_2 adsorption performance and sulfur tolerance. Increasing the coverage of the dopants further strengthened NO_2 adsorption in all cases except Ca-doped BaO (100) surface. In spite of the lack of insight from charge transfer, the geometric parameters enabled partial explanation for the variations in the adsorption energies.

Even though (100) alkali metal oxide surface is not a stoichiometric surface and the surface

energy cannot be easily calculated, a small set of adsorption geometries were tested on this surface. The binding energies of the NO_2 adsorption configurations were higher than the binding energies of the SO_2 adsorption configurations. As the basicity of the alkali metal increases from Li_2O to K_2O, the binding energies of the SO_2 adsorption configurations increase as well. By the light of this information, it can be concluded that the alkali metal oxide (100) surface is an adequate storage material for the NSR catalysts and the Li_2O (100) surface is the most adequate one. For the case of the (110) surface, the adsorption energies of the NO_2 binding configurations decreased as the adsorption energies of the SO_2 binding configurations increased. Only the K_2O (110) surface was found to be promising since the stability of the NO_2 adsorption on this surface is competing with the stability of SO_2 adsorption.

In the case of the alkali metal-loaded TiO_2 (001) surface, the stability of all of the NO_2 adsorption geometries were higher than the stability of the SO_2 adsorption geometries. The highest adsorption energy for the NO_2 and SO_2 adsorption was obtained on the K included TiO_2 (001) surface. This result indicates that increasing basicity enhances both the adsorption of the NO_2 and SO_2.

REFERENCES

[1] J. A. Botas, M. A. Gutierrez-Ortiz, M. P. Gonzalez-Marcos, J. A. Gonzalez-Marcos, J. R. Gonzalez-Velasco, *Appl. Catal. B-Environ.* **32**, 243 (2001).

[2] C. K. N. Patel, E. G. Burkhardt, C. A. Lambert, *Science* **184**, 1173 (1974).

[3] K. D. Karlin, *Progress in Inorganic Chemistry* (Wiley, 2007).

[4] R. Impens, *Stud. Surf. Sci. Catal.* **30**, 11 (1987).

[5] D. Mauzerall, B. Sultan, N. Kim, D. F. Bradford, *Atmos. Environ.* **39**, 2851 (2005).

[6] S. Roy, M. S. Hegde, G. Madras, *Applied Energy* **86**, 2283 (2009).

[7] V. Vestreng, K. Mareckova, S. Kakareka, A. Malchykhina, T. Kukharchyk, *EMEP Technical Report* **1** (2007).

[8] Euro 5 Emissions Standards for Cars, http://www.euractiv.com/en/transport/euro-5-emissions-standards-cars/article-133 325 Last accessed on 5 June 2011.

[9] V. Vestreng, L. Ntziachristos, A. Semb, S. Reis, I. S. A. Isaksen, L. Tarrason, *Atmos. Chem. Phys.* **9**, 1503 (2009).

[10] L. Castoldi, L. Lietti, P. Forzatti, S. Morandi, G. Ghiotti, F. Vindigni, *Journal of Catalysis* **276**, 335 (2010).

[11] N. Takahashi, H. Shinjoh, T. Iijima, T. Suzuki, K. Yamazaki, K. Yokota, H. Suzuki, N. Miyoshi, S. Matsumoto, T. Tanizawa, T. Tanaka, S. Tateishi, K. Kasahara, *Catalysis Today* **27**, 63 (1996).

[12] J. J. Yu, J. Cheng, C. Y. Ma, H. L. Wang, L. D. Li, Z. P. Hao, Z. P. Xu, *Journal of Colloid and Interface Science* **333**, 423 (2009).

[13] A. Lucas-Consuegra, A. Caravaca, P. Sanchez, F. Dorado, J. L. Valverde, *Journal of Catalysis* **259** 54 (2008).

[14] F. Prinetto, G. Ghiotti, I. Nova, L. Lietti, E. Tronconi, P. Forzatti, *J. Phys. Chem. B* **105**, 12372 (2001).

[15] F. Prinetto, M. Manzoli, S. Morandi, F. Frola, G. Ghiotti, L. Castoldi, L. Lietti, P. Forzatti, *J. Phys. Chem. C* **114**, 1127 (2010).

[16] S. M. Park, J. W. Park, H. Ha, H. Han, G. Seo, *Journal of Molecular Catalysis A: Chemical* **273**, 64 (2007).

[17] L. Olsson, H. Persson, E. Fridell, M. Skoglundh, B. Andersson, *J. Phys. Chem. C* **105**, 6898 (2001).

[18] J. Szanyi, J. H. Kwak, D. H. Kim, S. D. Burton, C. H. F. Peden, *J. Phys. Chem. B* **109**, 27 (2005).

[19] P. Broqvist, I. Panas, E. Fridell, H. Persson, *J. Phys. Chem. B* **106**, 137 (2002).

[20] P. Broqvist, H. Grönbeck, E. Fridell, I. Panas, *Catalysis Today* **96**, 71 (2004).

[21] E. J. Karlsen, M. A. Nygren, L. G. M. Pettersson, *J. Phys. Chem. B* **107**, 7795 (2003).

[22] M. M. Branda, C. D. Valentin, G. Pacchoni, *J. Phys. Chem. B* **108**, 4752 (2004).

[23] H. Grönbeck, P. Broqvist, I. Panas, *Surface Science* **600**, 403 (2006).

[24] E. Fridell, H. Persson, B. Westerberg, L. Olsson, M. Skoglundh, *Catalysis Letters* **66**, 71 (2000).

[25] L. Cheng, Q. Ge, *J. Phys. Chem. C* **112**, 16924 (2008).

[26] J. H. Kwak, D. Mei, C. Yi, D. H. Kim, C. H. F. Peden, L. F. Allard, *Journal of Catalysis* **261**, 17 (2009).

[27] P. Broqvist, H. Grönbeck, E. Fridell, *J. Phys. Chem. B* **108**, 3526 (2004).

[28] M. Tutuianu, O. R. Inderwildi, W. G. Bessler, J. Warnatz, *J. Phys. Chem. B* **110**, 17484 (2006).

[29] P. J. Schmitz, R. J. Baird, *J. Phys. Chem. B* **106**, 4172 (2002).

[30] M. Piacentini, M. Maciejewski, A. Baiker, *Appl. Catal. B* **72**, 105 (2007).

[31] D. H. Kim, Y. H. Chin, G. G. Muntean, A. Yezeretz, N. W. Currier, W. S. Epling, H. Y. Chen, H. Hess, C. H. F. Peden, *Ind. Eng. Chem. Res.* **45**, 8815 (2006).

[32] D. H. Kim, J. H. Kwak, J. Szanyi, X. Wang, G. Li, J. C. Hanson, C. H. F. Peden, *J. Phys. Chem. C* **113**, 21123 (2009).

[33] M. Born, R. Oppenheimer, *Ann. Phys.* **84**, 457 (1927).

[34] P. Hohenberg, W. Kohn, *Phys. Rev.* **136**, B864 (1964).

[35] W. Kohn, L. J. Sham, *Phys. Rev.* **140**, A1133 (1965).

[36] J. P. Perdew, K. Burke, and M. Ernzerhof, *Phys. Rev. Lett.* **77**, 3865 (1996).

[37] A. D. Becke, *Phys. Rev. A* **38**, 3098 (1988).

[38] C. Lee, W. Yang and R. G. Parr, *Phys. Rev. B* **37**, 785 (1988).

[39] X. Gonze, F. Finocchi, *Physica Scripta.* **T109**, 40 (2004).

[40] D. R. Hamann, M. Schlüter, C. Chiang, *Phys. Rev. Lett.* **430**, 1494 (1979).

[41] D. Vanderbilt, *Phys. Rev. B* **41**, 7892 (1990).

[42] Quantum ESPRESSO, http://www.quantum-espresso.org/ Last accessed on 22 July 2011.

[43] M. Andonova, G. S. Şentürk, E. Kayhan, E. Ozensoy, *J. Phys. Chem. C* **113**, 11014 (2009).

[44] R. W. G. Wyckoff, *Crystal Structures* (Wiley, 1963).

[45] W. F. Schneider, *J. Phys. Chem. B* **108**, 273 (2004).

[46] E. Zintl, A. Harder, B. Dauth, *Z. Elektrochem.* **40**, 588 (1934).

[47] Z. Cancarevic, J. C. Schon, M. Jansen, *Phys. Rev. B* **73**, 224114 (2006).

[48] M. S. Palmer, M. Neurock, M. M. Olken, *J. Phys. Chem. B* **106**, 6543 (2002).

[49] M. Lazzeri, A. Vitttadini, A. Selloni, *Phys.Rev B* **63**, 155409 (2001).

[50] R. Hummatov, *Effect of Support Material in NO_x Storage/Reduction Catalysts*, METU, Ankara, (2010).

[51] J. K. Burdett, T. Hughbanks, G. J. Miller, J. W. Richardson, Jr., J. V. Smith, *J. Am. Chem. Soc.* **109**, 3639 (1987).

[52] D. R. Lide, *CRC Handbook of Chemistry and Physics* (CRC Press, 2005-6).

[53] N. N. Greenwood, A. Earnshaw, *Chemistry of the Elements* (Pergammon Press, 1997).

[54] M. Calatayud, C. Minot, *Surf. Sci.* **552**, 169 (2004).

[55] P. Broqvist, I. Panas, H. Grönbeck, *J. Phys. Chem. B* **109**, 15410 (2005).

[56] A. Lichanot, M. Gelize, C. Larrieu, C. Pisani, *J. Phys. Chem. Solids* **52**, 1155 (1991).

[57] M. Springborg, *Methods of electronic-structure calculations: from molecules to solids*, (Jhon Wiley, 2000).

[58] T. J. Toops, N. A. Ottinger, C. Liang, J. A. Pihl, E. A. Payzant, *Catalysis Today* **160**, 131 (2011).

[59] P. Pyykkö, M. Atsumi, *Chem. Eur. J.* **15**, 186 (2009).